AFRL-RQ-WP-TR-2020-0099

EVOLUTION OF ELECTRON PROPERTIES AFTER NANOSECOND, REPETITIVELY PULSED DISCHARGES IN AIR MEASURED BY THOMSON SCATTERING

Chase Murray, Steven Adams, and Jared Miles

Electrical Systems Branch
Power and Control Division

OCTOBER 2020
Interim Report

DISTRIBUTION STATEMENT A. Approved for public release.
Distribution is unlimited.

STINFO COPY

AIR FORCE RESEARCH LABORATORY
AEROSPACE SYSTEMS DIRECTORATE
WRIGHT-PATTERSON AIR FORCE BASE, OH 45433-7542
AIR FORCE MATERIEL COMMAND
UNITED STATES AIR FORCE

NOTICE AND SIGNATURE PAGE

Using Government drawings, specifications, or other data included in this document for any purpose other than Government procurement does not in any way obligate the U.S. Government. The fact that the Government formulated or supplied the drawings, specifications, or other data does not license the holder or any other person or corporation; or convey any rights or permission to manufacture, use, or sell any patented invention that may relate to them.

This report was cleared for public release by the USAF 88th Air Base Wing (88 ABW) Public Affairs Office (PAO) and is available to the general public, including foreign nationals.

Copies may be obtained from the Defense Technical Information Center (DTIC) (https://discover.dtic.mil/).

AFRL-RQ-WP-TR-2020-0099 HAS BEEN REVIEWED AND IS APPROVED FOR PUBLICATION IN ACCORDANCE WITH ASSIGNED DISTRIBUTION STATEMENT.

This report is published in the interest of scientific and technical information exchange and its publication does not constitute the Government’s approval or disapproval of its ideas or findings.

REPORT DOCUMENTATION PAGE

Form Approved
OMB No. 0704-0188

The public reporting burden for this collection of information is estimated to average 1 hour per response, including the time for reviewing instructions, searching existing data sources, gathering and maintaining the data needed, and completing and reviewing the collection of information. Send comments regarding this burden estimate or any other aspect of this collection of information, including suggestions for reducing this burden, to Department of Defense, Washington Headquarters Services, Directorate for Information Operations and Reports (0704-0188), 1215 Jefferson Davis Highway, Suite 1204, Arlington, VA 22202-4302. Respondents should be aware that notwithstanding any other provision of law, no person shall be subject to any penalty for failing to comply with a collection of information if it does not display a currently valid OMB control number. **PLEASE DO NOT RETURN YOUR FORM TO THE ABOVE ADDRESS**.

1. REPORT DATE *(DD-MM-YY)*	2. REPORT TYPE	3. DATES COVERED *(From - To)*
October 2020	Interim	10 June 2019 – 21 August 2020

4. TITLE AND SUBTITLE
EVOLUTION OF ELECTRON PROPERTIES AFTER NANOSECOND, REPETITIVELY PULSED DISCHARGES IN AIR MEASURED BY THOMSON SCATTERING

5a. CONTRACT NUMBER
In-house

5b. GRANT NUMBER

5c. PROGRAM ELEMENT NUMBER
62203F

6. AUTHOR(S)
Chase Murray, Steven Adams, and Jared Miles

5d. PROJECT NUMBER
3145

5e. TASK NUMBER

5f. WORK UNIT NUMBER
Q235

7. PERFORMING ORGANIZATION NAME(S) AND ADDRESS(ES)
Electrical Systems Branch (AFRL/RQQE)
Power and Control Division
Air Force Research Laboratory, Aerospace Systems Directorate
Wright-Patterson Air Force Base, OH 45433-7542
Air Force Materiel Command, United States Air Force

8. PERFORMING ORGANIZATION REPORT NUMBER
AFRL-RQ-WP-TR-2020-0099

9. SPONSORING/MONITORING AGENCY NAME(S) AND ADDRESS(ES)
Air Force Research Laboratory
Aerospace Systems Directorate
Wright-Patterson Air Force Base, OH 45433-7542
Air Force Materiel Command
United States Air Force

10. SPONSORING/MONITORING AGENCY ACRONYM(S)
AFRL/RQQE

11. SPONSORING/MONITORING AGENCY REPORT NUMBER(S)
AFRL-RQ-WP-TR-2020-0099

12. DISTRIBUTION/AVAILABILITY STATEMENT
DISTRIBUTION STATEMENT A. Approved for public release. Distribution is unlimited.

13. SUPPLEMENTARY NOTES
PA Clearance Number: 88ABW-2020-2579; Clearance Date: 28 Jul 2020.

This technical paper is the result of in-house research conducted at the WPAFB facilities of AFRL/RQQE and constitutes Chase Murray's master's thesis for the Physics Department at Wright State University.

14. ABSTRACT

This work was an investigation of nanosecond repetitively pulsed discharges in air by measuring the evolution of electron density and electron temperature between pulses using Thomson scattering of laser light. Bursts of repetitive pulses within several microseconds after the initial pulse were found to exhibit a coupling effect and create an even higher electron density than the initial pulse. The wide range of temperatures and densities of the electrons existing between pulses allow an opportunity to explore both the collective and non-collective regimes of Thomson scattering. By measuring electron density and temperature at a variety of times, an accurate description of the coupling between discharges can been formulated which provides insight into the behavior and potential applications of nanosecond repetitive pulse discharges.

15. SUBJECT TERMS
nanosecond pulse, air discharge, electron density, electron temperature, Thomson scatter

16. SECURITY CLASSIFICATION OF:			17. LIMITATION OF ABSTRACT:	18. NUMBER OF PAGES	19a. NAME OF RESPONSIBLE PERSON (Monitor)
a. REPORT	b. ABSTRACT	c. THIS PAGE			Steven F. Adams
Unclassified	Unclassified	Unclassified	SAR	52	19b. TELEPHONE NUMBER (Include Area Code) N/A

TABLE OF CONTENTS

DISTRIBUTION STATEMENT A. Approved for public release. Distribution is unlimited.

LIST OF FIGURES

Figure **Page**

DISTRIBUTION STATEMENT A. Approved for public release. Distribution is unlimited.

DISTRIBUTION STATEMENT A. Approved for public release. Distribution is unlimited.

LIST OF TABLES

Table **Page**

DISTRIBUTION STATEMENT A. Approved for public release. Distribution is unlimited.

1. Summary

This work was an investigation of nanosecond repetitively pulsed discharges in air by measuring the evolution of electron density and electron temperature between pulses using Thomson scattering of laser light. Bursts of repetitive pulses within several microseconds after the initial pulse were found to exhibit a coupling effect and create an even higher electron density than the initial pulse. The wide range of temperatures and densities of the electrons existing between pulses allow an opportunity to explore both the collective and non-collective regimes of Thomson scattering. By measuring electron density and temperature at a variety of times, an accurate description of the coupling between discharges can been formulated which provides insight into the behavior and potential applications of nanosecond repetitive pulse discharges.

DISTRIBUTION STATEMENT A. Approved for public release. Distribution is unlimited.

2. Introduction

2.1 Plasma

A plasma is formed of two parts: a gas of ions and their freed electrons. First described by Langmuir, plasmas have been widely studied in various forms. The sun is an example of a fully ionized plasma, while most plasmas on Earth consist of a partially ionized gas with ions and electrons equally distributed throughout neutral molecules or atoms. Plasma is sometimes referred to as a fourth state of matter as the collective electrostatic and magnetic interactions between charged particles throughout the plasma are unique with no analogue to ordinary gases, liquids, or solids. Plasma occurs naturally in interstellar media, the solar wind, aurorae in Earth's magnetosphere [1], and lightning within Earth's atmosphere [2]. Scientists and engineers have found applications for plasmas that have tremendously benefited society, such as lighting and displays [3], plasma cleaning and decontamination [4], plasma wound healing [5], materials processing [6, 7], microwave sources [8], space thruster propulsion [9], plasma cutting and welding [10], and high power switches [11]. Plasmas created in air under standard atmospheric conditions will typically extinguish within a relatively short period of time due to collisional recombination of the charged particles unless a continuous excitation field is present to promote ionization and sustain the charge density. This is why lightning bolts and smaller sparks due to electrostatic build up will form plasmas in the Earth's atmosphere for only a very short duration. Man-made plasmas that are more continuous, such as an arc welding plasma or a fluorescent lighting tube, require a continuous source of high voltage to sustain the plasma.

The plasma source studied in this work generates repetitive high voltage nanosecond pulse discharges in air between two metal pin electrodes, as seen in the photograph in Figure 1, where the short duration high voltage pulse efficiently creates a high charge density despite a relatively low input energy.

Figure 1: Single nanosecond pulse discharge within a pin-to-pin electrode separation of 2 mm

This type of nanosecond pulse discharge is being investigated for enhanced ignition and combustion systems in internal combustion engines and aerospace propulsion systems where the short duration pulses produce both the excited species and the gas temperature increase necessary for successful ignition with reduced discharge power [12].

In the quest to understand the complex behavior of plasma systems and to benefit from new applications of plasma science, it is essential to study the electrical characteristics of a plasma in the form of its charge density and the energy content, or temperature, of the charge distribution. A plasma generally has two primary subsets of interacting charge particles: electrons and positive ions, although negative ions could also play a role. In a quasi-neutral plasma, it is often assumed that the electron density and positive ion density are equal. The electrons are more mobile due to their much lower mass and will often acquire a much greater average kinetic energy from an excitation field than the ions. The electron temperature value will therefore

DISTRIBUTION STATEMENT A. Approved for public release. Distribution is unlimited.

typically be much higher than that of the ions or neutral species. This difference in temperatures between species is one aspect that would classify a plasma as being in a non-equilibrium state.

In a plasma, although free electrons are not bound to their ions, some influence is still felt from the electric field of the neighboring ions. Similar to a mass on a spring, if the electrons are displaced slightly with respect to the ions, a restoring force will pull them back toward their equilibrium position, but then the electrons will overshoot before being pulled back in the opposite direction. The rate at which this pattern repeats is referred to as the plasma frequency, ω_p, which will depend on the electron density, n_e.

On a small scale, the electrostatic effects of each individual charge will extend outward to interact with neighboring charges, although the electric potential drops off as $1/r$. At larger scales, the collective effects of the charge distribution tend to cancel out the effective electric potential of individual charges. The limit of the distance over which the influence of the electrostatic effects of individual charges can be felt is known as the Debye length, λ_D. Generally, λ_D will decrease as n_e increases, meaning that a more dense plasma will leave less room for individual charge effects and the plasma will more likely behave collectively as a distribution of charge.

If a disturbance in the plasma, such as a charge perturbation or an imposed oscillating electric field, was extended over a length equal to or greater than the Debye length, then the effects of the disturbance would be experienced collectively by the plasma. On the other hand, if the disturbance was over a length less than the Debye length, then effects would be experienced by the individual charges, or non-collectively. The experiments in this work involve the scatter of laser photons from the plasma, so a rough indication of whether the photon scattering will be a collective or non-collective disturbance within the plasma is whether the incident laser wavelength, λ_i is significantly greater than or less than the Debye length, respectively, as illustrated in Figure 2.

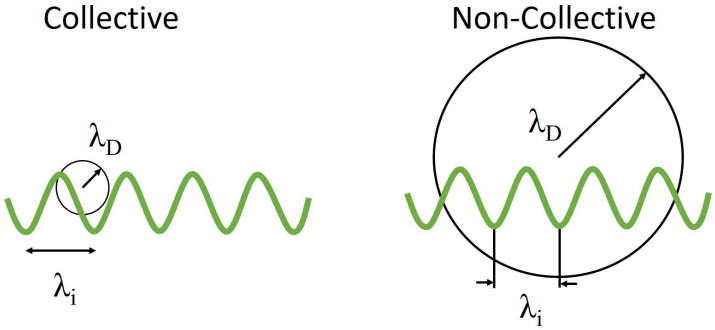

Figure 2: Light wave interacting with small Debye sphere in dense plasma and larger Debye sphere in less dense plasma where Thomson scattering will exhibit collective and non-collective behavior, respectively

2.2 Scattering

2.2.1 Thomson Scattering

Thomson scattering is absorption and re-emission of electromagnetic radiation from charged particles. When the incident light is from a unidirectional, monochromatic, coherent, linearly polarized laser source the interpretation of the resulting Thomson scattering spectrum yields information on electron density and temperature in the laser interaction region. Thomson

DISTRIBUTION STATEMENT A. Approved for public release. Distribution is unlimited.

scattering was first explained by J.J. Thomson in 1906 [13], where Thomson derived the behavior of low energy elastic collisions of electromagnetic waves with charged particles using a classical interpretation. As described earlier, the disturbance caused by electromagnetic radiation in Thomson scattering may involve a non-collective behavior when $\lambda_D \ll \lambda_i$ or a collective behavior when $\lambda_D \ll \lambda_i$. Thomson's early classical approximation only holds true for sufficiently long wavelengths of radiation interacting with an individual charged particle, and thus corresponds to the non-collective scattering case. In the classical interpretation, the oscillating electric field of the wave interacts with a charged particle. The charged particle itself begins to oscillate due to the force applied by the radiation field. The oscillating charged particle in turn generates its own scattered electromagnetic waves that radiate in all directions.

Analysis of the wavelength spectrum of Thomson scattering is the key to deriving electron temperature and density information from an experiment. For an electron that is stationary in the reference frame of the radiation source and the scatter detector, the wavelength of the scattered photon will be identical to that of the incident photon. However, most electrons will have some initial velocity relative to the laboratory frame of reference and the scattered radiation will experience a shift from a double Doppler effect, with one effect from the incident light from the source approaching the moving electron and the other effect from the emission in the direction of the detector from the moving electron.

Now consider a source of many photons of light scattering non-collectively from many electrons in a plasma, where each scattered photon will have a wavelength shift based on the velocity of the electron it encountered. The profile of wavelength shifts of the scattered light will depend directly on the distribution of velocities of the electrons. For a group of electrons with a typical Maxwellian velocity distribution, the corresponding Doppler shifts can be shown to create a scattered wavelength spectrum that has a Gaussian shape. Thus, the non-collective scattering case results in a Gaussian shaped spectrum with a spectral width from which the electron temperature of the plasma can be directly calculated. The electron density of a plasma can also be derived from a non-collective Thomson scattering spectrum, although additional calibration measurements are required from Raman scattering, which will be discussed later.

Conditions for collective Thomson scattering, on the other hand, with $\lambda_D \ll \lambda_i$ can be brought about by a relatively high electron density causing a reduced Debye length. In collective scattering, the scattered radiation experiences constructive and destructive interference effects due to the combination of contributions of each electron. Relative phase shifts between photons scattered from electrons with large scale positional patterns within the plasma cause interference patterns in the scatter spectrum that is related to the plasma frequency. The collective scatter wavelength spectrum is a more complex saddle-like shape centered about the incident wavelength, with the position and shape of the side peaks depending on the plasma frequency. Although the collective spectrum is more complex than the non-collective case, its dependence on plasma frequency means that both the electron density and electron temperature of a plasma can be determine solely by a fit of the collective spectrum shape. Examples of both non-collective and collective Thomson scattering spectral profiles are shown in Figure 3.

DISTRIBUTION STATEMENT A. Approved for public release. Distribution is unlimited.

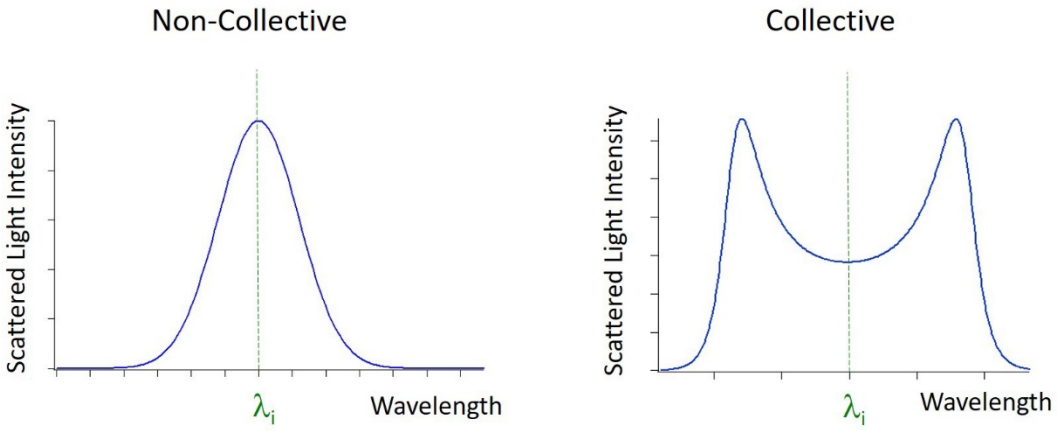

Figure 3: Typical shapes of Thomson scattering spectra for non-collective and collective behavior

2.3 Rayleigh/Raman Scattering

When conducting Thomson scattering experiments within a plasma, neutral molecules as well as electrons will scatter the incident light and must also be considered when analyzing the scattered light spectrum. Rayleigh and Raman scattering are the other primary signals that must be contended with during Thomson measurements. While the Rayleigh signal is generally unwanted, the Raman signal can be used for calibration of Thomson measurements.

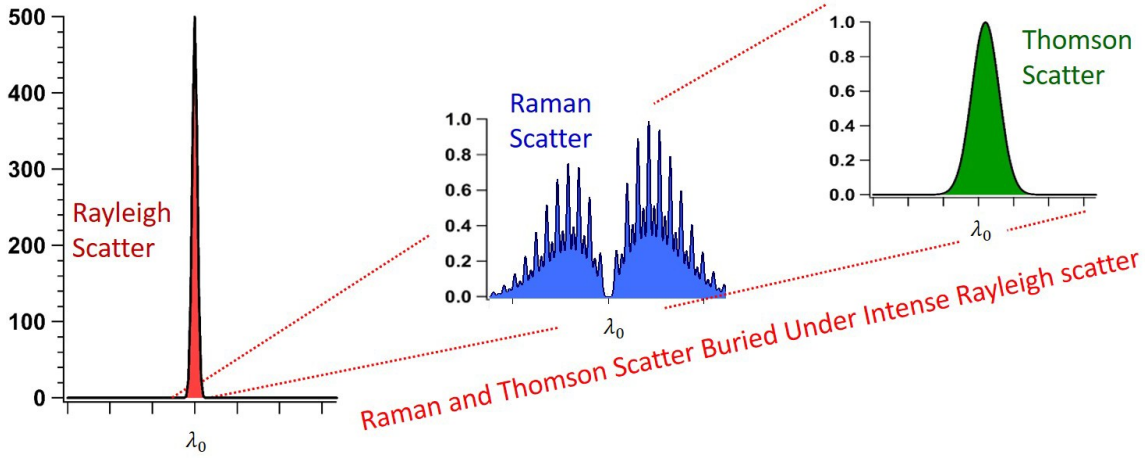

Figure 4: Diagram of Rayleigh, Raman, and Thomson components of scattering spectrum.

Rayleigh scattering is a relatively intense elastic scattering of incident radiation from neutral molecules and was first described by Lord Rayleigh (a.k.a. John William Strutt) in the 1870s. Due to the elastic nature of Rayleigh scattering, the scattered photons have identical wavelengths to the incident photons. The intensity of the Rayleigh scattered light typically overwhelms weaker scattering signals making Thomson scattering nearly impossible to detect. Special instruments, such as the masked triple grating spectrometer (TGS), have been developed that block and remove a narrow band of light from the laser scatter spectrum around the incident laser wavelength, thus removing the Rayleigh scatter wavelength while preserving most of the Thomson spectrum.

Raman scattering is an inelastic scattering from neutral molecules and was first described in the 1920s by Chandrashekhara Venkata Raman. In Raman scattering, a molecule absorbs an incident photon and enters a higher excited virtual energy state. As the molecule falls from this excited

DISTRIBUTION STATEMENT A. Approved for public release. Distribution is unlimited.

state, it radiates a scattered photon. An excited molecule may fall back to a higher energy level than which it initially started (Stokes Raman scattering) or a lower energy level (anti-Stokes Raman scattering). This process emits a scattered photon of higher or lower wavelength, respectively, than the incident photon. The shifted peaks of the rotational Raman spectrum in air can be predicted very accurately from the known spectroscopic constants of molecular nitrogen and oxygen and the intensity distribution of the peaks can be predicted from the temperature of the gas. A diagram showing the general shapes of Rayleigh, Raman, and Thomson scatter spectra as well as demonstrating the dominant intensity of Rayleigh scattering is shown in Figure 4.

Analyzing the rotational Raman scatter spectrum along with a Thomson scatter spectrum has been found to be of great use for calibration. The well known Raman spectral shifts for nitrogen and oxygen insure that the wavelength axis of the Thomson scatter analysis is extremely accurate. More importantly, by comparing the intensity ratio of the Raman signal in standard density air to any Thomson signal intensity using the same radiation source and detector, and using a known ratio between the Raman cross section and the Thomson cross section, the absolute electron density can be calculated.

2.4 Electron Properties of Nanosecond Discharge

For this work, electron density and temperature measurements were taken following a single high voltage pulse discharge as well as following multiple pulse discharges applied at high frequency. The nanosecond duration pulses had peak voltages up to 15 kV and were applied to a 2 mm gap pin-to-pin discharge configuration open to atmospheric air conditions. Electron densities and electron temperatures were measured via Thomson scattering with a 532 nm laser for multiple times following the discharge, with collective scattering analysis required early after the pulse and non-collective scattering analysis applied at later times.

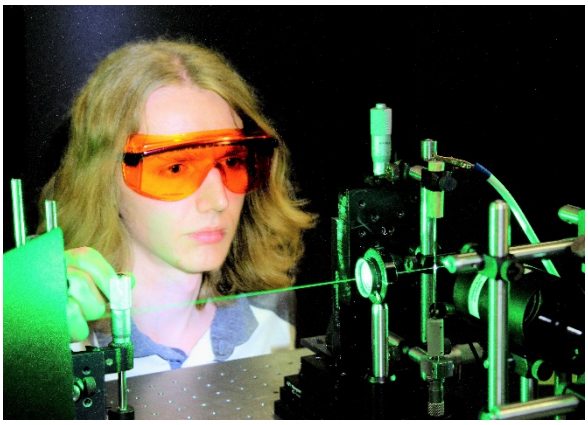

Figure 5: Chase Murray conducting research at the Air Force Research Laboratory facilities at Wright-Patterson AFB, OH

DISTRIBUTION STATEMENT A. Approved for public release. Distribution is unlimited.

3. Theory

3.1 Plasma Properties

The two primary measurements of plasma properties in this work were electron temperature and electron density. The electron temperature within a plasma is the thermodynamic temperature of the bulk free electrons which is directly proportional to the mean average kinetic energy of the electrons' translational motion. The mean kinetic energy of electrons with three dimensions of freedom would be $E = 3/2 k_B T_e$, where k_B is the Boltzmann constant of 1.381×10^{-23}J/K or 8.617×10^{-5}eV/K. Thus, the temperature of the electron SI units of Kelvin would be

$$T_e = \frac{1}{k_B} 2/3 \langle E \rangle. \tag{1}$$

As mentioned earlier, this electron temperature in a plasma is often very high, in the range of tens of thousands of Kelvin, and thus plasma physicists have adopted a vernacular of expressing electron temperature in proportional units of energy as electron volts, or eV, which results in more reasonable numerical values. This common conversion, although not aligned with SI unit standards, is done by simply suppressing the Boltzmann constant, allowing the electron temperature to be expressed in the proportional energy unit of eV as

$$T_e = 2/3 \langle E \rangle. \tag{2}$$

It should be noted that in this document, wherever T_e is used in an equation to derive a theoretical expression, it carries the proper SI units of Kelvin, but when experimental measurements are presented, T_e will be expressed in units of eV.

The electron density, n_e, investigated in this work is the number of electrons per unit volume in a plasma, not be confused with the quantum physics term of electron density referring to the probability of finding an electron at a particular point in space. As discussed earlier, disturbances in a quasi-neutral distribution of electrons and ions will cause the bulk electrons to oscillate at a frequency referred to as the plasma frequency, ω_p. This plasma frequency will depend on the electron density as

$$\omega_p = \sqrt{\frac{n_e e^2}{m^* \varepsilon_0}} \tag{3}$$

where e is the fundamental charge, m^* is the effective mass of the electron and ε_0 is the permittivity of free space.

Both the electron temperature and the electron density factor into a critical plasma length parameter called the Debye length, which defines a spherical volume around a charge which effectively screens the charge's electrostatic effects from outside this volume. By defining one Debye length as the distance from a central charge in which the electric potential drops by a factor of $1/e$, then the Debye length can be expressed as

DISTRIBUTION STATEMENT A. Approved for public release. Distribution is unlimited.

$$\lambda_D = \sqrt{\frac{\varepsilon_0 k_B T_e}{e^2 n_e}}. \tag{4}$$

The Debye lengths for the air discharges in this study tended to be in the range of 10^{-8} m to 10^{-5} m. The 532 nm laser probe used for this study, being on the order of 10^{-7} m, induced an electromagnetic disturbance over a length that was both greater than or less than the Debye length at different times throughout the experiment.

3.2 General Scattering

Light scattering occurs when atoms, molecules, or electrons absorb electromagnetic radiation and re-emit the radiation in various directions and intensities. Radiation re-emitted from particles in the laser path may be scattered in any direction in three dimensions away from the particle, although a relatively small solid angle is often chosen in experiments to observe the scatter. In this work, a laser beam shines through a gaseous region of interest. The volume where the laser passes through the gas can be approximated as a cylinder with a circular cross-sectional area, A. The incident laser is treated as uniform over that area. Within the volume of this cylinder there are N number of particles. Each of these particles have a probability that it will scattering some of the laser light, with that probability represented by a cross section, σ, with a unit of area. Since the laser is unidirectional, only the cross-sectional area of these particles in the direction of the laser beam matter. The concept of the laser cylinder and particle cross sections are illustrated in Figure 6.

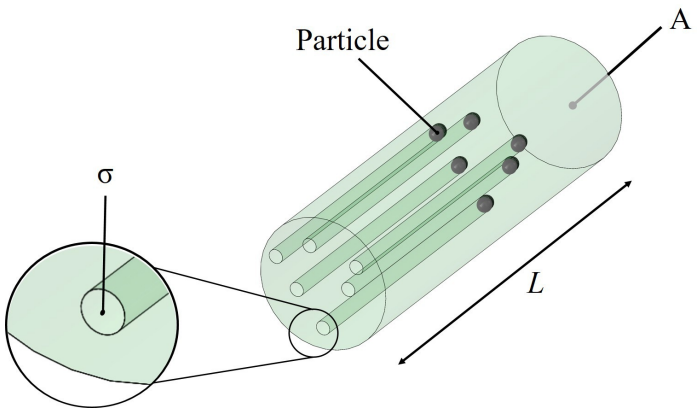

Figure 6: The volume of interest consists of a cylindrical laser beam passing through N number of particles each with cross section σ.

The number of particles, N, can also be expressed in terms of number density as nV, where V is the cylinder volume, or nAL, where L is the length of the cylinder. The total cross section which the laser light experiences when passing through the cylinder is then

$$\sigma_{Tot} = N\sigma = nV\,\sigma = nAL\sigma. \tag{5}$$

When shining laser power P_i through the cylinder of gas, typical σ_{Tot} values dictate that only a small fraction of the laser light is scattered. The total amount of light power that is scattered from the particles in the cylinder in all directions, P_s^{Tot}, can be expressed as

DISTRIBUTION STATEMENT A. Approved for public release. Distribution is unlimited.

$$P_s^{Tot} = P_i \times [\%\ \text{Scattered}] = P_i \frac{\sigma_{Tot}}{A} = P_i \frac{nAL\sigma}{A} = P_i nL\sigma. \tag{6}$$

The amount of radiant scatter power collected by a detector within a certain solid angle $\Delta\Omega$ is given by P_s and is proportional to the differential cross section, $d\sigma/d\Omega$, for that scatter direction as

$$P_s = P_i nL \frac{d\sigma}{d\Omega} \Delta\Omega \tag{7}$$

which assumes that $\Delta\Omega$ is small enough that $d\sigma/d\Omega$ doesn't change much across it.

While this equation works well for the collected scatter power at all wavelengths, in order to conduct a spectral analysis of the scatter, interest is focused on scatter power as a function of scatter wavelength, λ_s. To do this the spectral density function is introduced, $S(\Delta\lambda)$, where $\Delta\lambda$ is the difference between the scattered and incident wavelengths. The shape of the spectral density function determines the spectral profile of wavelengths of the scattered power and is normalized as

$$\int_{-\infty}^{+\infty} S(\Delta\lambda) d\lambda_s = 1. \tag{8}$$

The scattered power as a function of wavelength can now be expressed as

$$P_s(\Delta\lambda) = LP_i \Delta\Omega n \frac{d\sigma}{d\Omega} S(\Delta\lambda). \tag{9}$$

This expression can be simplified by assuming a constant incident laser power and detector configuration and setting $C = LP_i\Delta\Omega$. This results in a general expression for the scattered power of

$$P_s(\Delta\lambda) = Cn \frac{d\sigma}{d\Omega} S(\Delta\lambda). \tag{10}$$

A laser passing through a plasma may generate a strong scatter power from more than one type of particle, i.e. from both neutral molecules and electrons. The different $P_s(\Delta\lambda)$ scatter signals from the different particles may overlap on the same detected spectrum. In this case it is notable that the constant C will be the same for each different signal, although n, $d\sigma/d\Omega$, and $S(\Delta\lambda)$ will likely be different for each. This relationship allows for a convenient calibration in this work by comparing Raman and Thomson scattering signals using the same laser and detector.

3.2.1 Raman Scattering

Although the analysis of Thomson scattering from electrons is primary to this work, Raman scattering from air molecules is an essential calibration technique and will be discussed first. Rotational Raman scatter from N_2 or O_2 involves absorption from an initial rotational J level to a virtual intermediate state and re-emission of radiation down to a final rotational J' level, and thus is a two-photon process. Photons have a spin angular momentum of $\pm\hbar$, or 1 quantum, so the selection rules dictate that the total change in spin can only be three possibilities: $\Delta J = 0$,

DISTRIBUTION STATEMENT A. Approved for public release. Distribution is unlimited.

resulting in elastic energy transfer (Rayleigh scattering), or $\Delta J = \pm 2$, resulting in inelastic energy transfer (Raman scattering).

Molecules at room temperature are typically in the ground vibrational state but populated to many different J energy levels due to thermal energy. Therefore many possible transitions from $J \rightarrow J'$ will be observed in room temperature air creating a rotational Raman spectrum with various peaks shifted from the incident wavelength. The profile of Raman Scattering consists of a series of scattering peaks due to each $J \rightarrow J'$ transition at wavelengths of $\lambda_{J \rightarrow J'}$. While each transition will scatter as described in the general scattering equation 10, the total Raman spectral profile will consist of the sum of every transition. The following derivation is taken primarily from the previously published work of van Gessel [14]. Rotational Raman scattering will consist of every $J \rightarrow J \pm 2$ transition with a scattered power of

$$P_R(\Delta\lambda) = C \sum_{J'=J\pm 2} n_J \frac{d\sigma_{J\rightarrow J'}}{d\Omega} S(\Delta\lambda - \lambda_{J\rightarrow J'}) \tag{11}$$

where the population density of each J level is n_J , the wavelength shift of the scattered radiation is $\Delta\lambda = \lambda_s - \lambda_i$, and differential cross sections $d\sigma_{J\rightarrow J}/d\Omega$ have been calculated previously [14, 15]. The spectral density function, $S(\Delta\lambda - \lambda_{J\rightarrow J})$, gives the spectral profile of each individual transition, which are determined primarily by instrument broadening.

For air molecules in thermal equilibrium, the density for each state J is

$$n_J = \frac{n_{\text{mol}}}{Q} \cdot g_J(2J+1) \exp\left[\frac{-BJ(J+1)}{k_B T_{\text{rot}}}\right] \tag{12}$$

where g_J is the statistical weight factor, T_{rot} is the rotational temperature, n_{mol} is the molecular density, B is a species' dependent rotational constant, and Q is the partition sum, approximated as

$$Q \approx \frac{k_B T_{\text{rot}}}{2B}(2I+1)^2 \tag{13}$$

where I is the nuclear spin quantum number.

The differential cross section depends on the angle of the collector with respect to the laser. In this experiment, scattering light was collected perpendicular to both the direction of the incident laser and the direction in which the incident laser was polarized.

In addition, the differential cross section for each transition also varies for each $J \rightarrow J'$ transition as well as properties of the gas and the laser wavelength. The differential cross section can be expressed in terms of $\lambda_{J\rightarrow J'}$ as

$$\frac{d\sigma_{J\rightarrow J'}}{d\Omega} = \frac{64\pi^4}{45\varepsilon_0^2} b_{J\rightarrow J'} \frac{\gamma^2}{\lambda_{J\rightarrow J'}^4} \tag{14}$$

DISTRIBUTION STATEMENT A. Approved for public release. Distribution is unlimited.

where γ is the anisotropy of the molecular polarizability tensor and $b_{J\to J'}$ is the Placzek-Teller coefficient. The coefficients for Stokes and Anti-stokes Raman scattering use

$$b_{J\to J-2} = \frac{3(J+1)(J+2)}{2(2J+1)(2J+3)},$$
$$b_{J\to J+2} = \frac{3J(J-1)}{2(2J+1)(2J-1)}.$$

In a purely perfect world, each rotational transition would produce a delta function. Due to a combination of broadening phenomena that is dominated by the spectrometer instrument broadening, each transition's spectral line is slightly blurred about its central wavelength. In this work, it is a good approximation to assign $S(\Delta\lambda)$ as a pseudo-Voigt, a function comprised of both a Lorentzian function, $L(\Delta\lambda)$, and a Gaussian function, $G(\Delta\lambda)$, summed together to represent the shape of these broadening effects. The parameter of full width at half maximum, Γ, is introduced to describe how wide the line is broadened as well as the parameter η to assign the ratio of Lorentzian to Gaussian effects. For each transition, the spectral density function is

$$S(\Delta\lambda) = \eta L(\Delta\lambda, \Gamma) + (1 - \eta)G(\Delta\lambda, \Gamma) \tag{15}$$

where the Gaussian and Lorentzian are defined in terms of Γ as

$$G(\Delta\lambda, \Gamma) = \frac{(2\ln 2)}{\Gamma\sqrt{\pi}} \exp\left[-\left(\frac{(2\ln 2)\Delta\lambda}{\Gamma}\right)^2\right],$$
$$L(\Delta\lambda, \Gamma) = \frac{(2\Gamma)}{\pi((\Delta\lambda)^2 + (2\Gamma)^2)}.$$

Different gas molecules produce unique scattering profiles due to differing J energy levels and differential cross sections. The total spectral profile in a gas mix will consist of the sum of each gas profile. For the typical laboratory air conditions in this work, only the contributions due to diatomic oxygen with $n_{\text{mol}} = 5 \times 10^{18}$ cm^{-3} and diatomic nitrogen $n_{\text{mol}} = 2 \times 10^{19}$ cm^{-3} were considered in the Raman scattering spectrum.

The constants used to simulate the Raman scattering spectra [14, 15] in this work are given in Table 1, which vary between even/odd J states.

An example experimental laser Raman spectrum in laboratory air is shown as both a raw image and a plot of vertically binned pixels along with a simulated fit using equation 11 and the constants from Table 1.

Table 1: Constants used for Raman scattering of 532 nm laser

Gas	g_J (Even J)	g_J (Odd J)	I	B (eV)	γ^2 (F^{2}m^4)
N2	3	6	1	2.467×10^{-4}	3.95×10^{-83}
O2	1	0	0	1.783×10^{-4}	1.02×10^{-82}

Fitting a Raman scattering spectrum in standard laboratory air with equation 11 allowed the determination of the constant C on a relative scale as

DISTRIBUTION STATEMENT A. Approved for public release. Distribution is unlimited.

$$C = \frac{P_R(\Delta\lambda)}{\sum_{J'=J\pm2} n_J \frac{d\sigma_{J\to J'}}{d\Omega} S(\Delta\lambda - \lambda_{J\to J'})} \tag{16}$$

so that a calibration could be conducted to determine absolute electron density from a Thomson scattering spectrum taken with the same instrument settings. An example of a good fit of a Raman scatter spectrum in air in this work is shown in Figure 7.

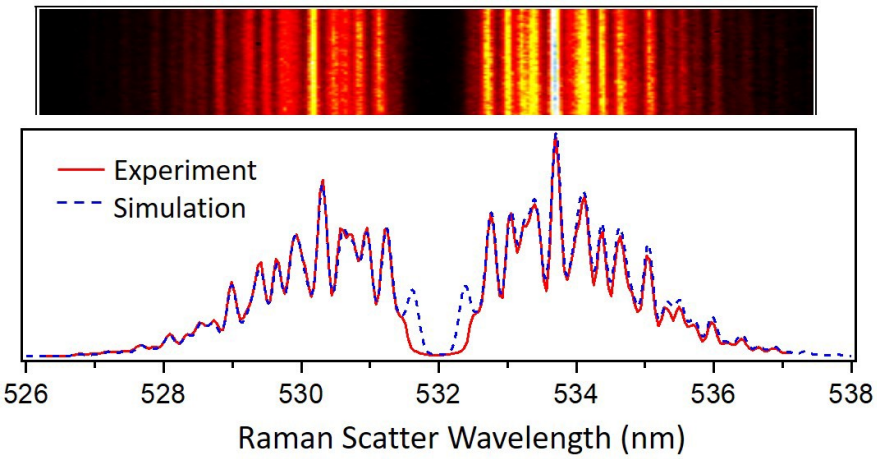

Figure 7: Example experimental spectral image and corresponding plot in laboratory air along with a fit of a theoretical simulation using equation 11

3.2.2 Thomson Scattering

In Thomson laser scattering, the electric field of the incident laser wave accelerates the charged particle, causing it to emit radiation and thus the wave is scattered. The classical analysis of Thomson scattering begins by treating the incident laser as an oscillating electromagnetic wave with wave vector $\mathbf{k}_i$ pointing along the x axis (from laser source to particle) and polarized as $\mathbf{E}_{i0}$ in the y-z plane, perpendicular to $\mathbf{k}_i$. The wave vector $\mathbf{k}_i$ thus identifies the direction of the incident radiation, but also the magnitude k_i is related to the incident laser wavelength, λ_i, and frequency, ω_i, as

$$k_i = \frac{2\pi}{\lambda_i} = \frac{\omega_i}{c}. \tag{17}$$

A portion of this incident wave interacts with charged particles in the laser path, and an electromagnetic wave is scattered in all directions. By placing a detector at some location away from the interaction region, a chosen direction can be designate to observe the scattered light as $\hat{\mathbf{s}}$. The wave vector $\mathbf{k}_s$ for the observed scattered radiation is also in the $\hat{\mathbf{s}}$ direction. Typically the scatter phenomenon results in the magnitudes $k_s \approx k_i$, although energy exchange with the moving electron during the interaction may result in a slight change in the scattered wave vector magnitude and accordingly the wavelength and frequency of the scatter, which are related as

$$k_s = \frac{2\pi}{\lambda_s} = \frac{\omega_s}{c}. \tag{18}$$

The slight difference between incident and scattered wave vectors is caused by a double Doppler shift. Because the thermal velocity of the electrons causes interactions with both the incident and

DISTRIBUTION STATEMENT A. Approved for public release. Distribution is unlimited.

the scattered radiation, a difference wave vector is identified as $\mathbf{k} = \mathbf{k}_s - \mathbf{k}_i$ to account for this combined effect and is defined as the vector difference between the wave vectors of the incident and scattering light. The magnitude of this difference wave vector is $k = |\mathbf{k}_s - \mathbf{k}_i| \approx 2k_i \sin(\theta/2)$, where θ is the angle between the incident wave vector $\mathbf{k}_i$ and the scatter wave vector $\mathbf{k}_s$. For $\theta = 90^\circ$, as used throughout this experiment, the difference wave vector will be $k = \sqrt{2}k_i$. The wave vectors, laser polarization, and angles between are shown in Figure 8 as a reference.

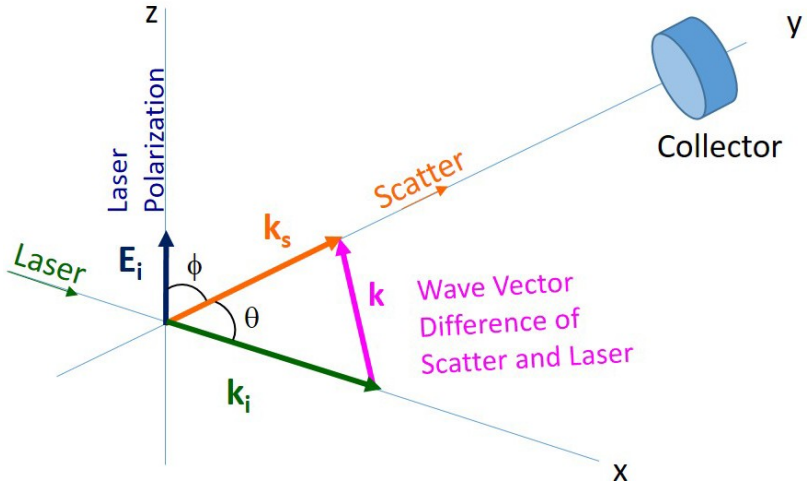

Figure 8: Diagram of wave vectors of laser and scattered radiation as well as laser polarization with associated angles shown vectors

The overall Doppler shift in the frequency, $\Delta\omega$, of any scattered photon will depend on the alignment of the difference wave vector, $\mathbf{k}$, with the velocity vector of the electron, $\mathbf{v}$, as

$$\Delta\omega = \omega_s - \omega_i = \mathbf{k} \cdot \mathbf{v} = kv_k \tag{19}$$

where v_k is the velocity component of the electron in the direction of $\mathbf{k}$. For the configuration in this experiment, the double Doppler frequency shift would then be $\Delta\omega = \sqrt{2}k_i v_k$ or can be expressed as

$$\frac{\Delta\omega}{\omega_i} = \sqrt{2}\,\frac{v_k}{c}. \tag{20}$$

It follows that the double Doppler wavelength shift would be

$$\frac{\Delta\lambda}{\lambda_i} = \frac{\sqrt{2}}{2}\,\frac{v_k}{c}. \tag{21}$$

To analyze the intensity of the Thomson scattered light, consider a single electron being accelerated by the oscillating polarization field, $\mathbf{E}_i$, of a laser according to

$$\dot{\mathbf{v}} = \frac{d\mathbf{v}}{dt} = -\frac{e}{m}\mathbf{E}_i \tag{22}$$

where $\dot{\mathbf{v}}$ is the acceleration of the electron. Jackson derives the electric field radiated by an accelerated change with non-relativistic speeds [16] as

DISTRIBUTION STATEMENT A. Approved for public release. Distribution is unlimited.

$$\mathbf{E}_s(\mathbf{r},t) = \frac{e}{4\pi\varepsilon_o c^2}\left[\frac{\hat{\mathbf{s}}\times(\hat{\mathbf{s}}\times\dot{\mathbf{v}})}{R}\right] = \frac{e^2}{4\pi\varepsilon_o mc^2}\left[\frac{\hat{\mathbf{s}}\times(\hat{\mathbf{s}}\times\mathbf{E}_{i0})}{R}\right]\cos\left(\mathbf{k}_i\cdot\mathbf{r}_p(t')-\omega_i t'\right) \tag{23}$$

where $\mathbf{r}$ is the displacement from the origin, $\hat{\mathbf{s}}$ is the unit vector in the scattering direction, R is the magnitude of the displacement vector from the scattering event, $\mathbf{E}_{i0}$ is the peak laser polarization field vector, and $\mathbf{r}_p$ is the electron position vector. A reference diagram of these displacement vectors is shown in Figure 9.

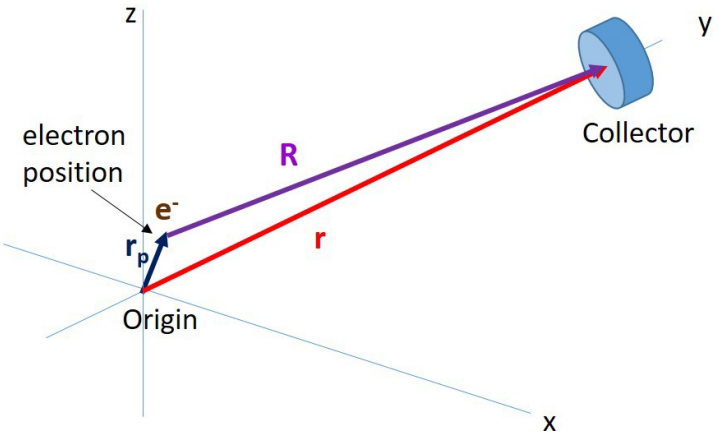

Figure 9: Displacement vectors involving the radiating electron position and the observation point or collector

The scattered radiation is detected at an observation point as distance R away at time t when scattered from the charge at a previous time $t' = t - R(t')/c$. The classical electron radius is known to be $r_e = e^2/(4\pi\varepsilon_o mc^2)$, which simplifies the scattered electric field to

$$\mathbf{E}_s(\mathbf{r},t) = \frac{r_e}{R}\left[\hat{\mathbf{s}}\times(\hat{\mathbf{s}}\times\mathbf{E}_{i0})\right]\cos\left(\mathbf{k}_i\cdot\mathbf{r}_p(t')-\omega_i t'\right). \tag{24}$$

By choosing the origin close to the electron and an observation point far away, such that $|\mathbf{r}| \approx R$ and $r_p \ll R$, it can be approximated that $R(t')$ only changes due to the electrons motion as $R(t') \approx R - \hat{\mathbf{s}}\cdot\mathbf{r}_p(t')$ and therefore

$$t' = t - \frac{R(t')}{c} \approx t - \frac{|R - \hat{\mathbf{s}}\cdot\mathbf{r}_p(t')|}{c}. \tag{25}$$

Also, by approximating the velocity of the electron as non-collisional and constant under small timescales such that $\mathbf{r}_p(t') \approx \mathbf{r}_p(0) + \mathbf{v}t'$, it can be substituted as

$$t' \approx \left[t - \frac{R}{c} - \frac{\hat{\mathbf{s}}\cdot\mathbf{r}_p(0)}{c} - \frac{\hat{\mathbf{s}}\cdot\mathbf{v}t'}{c}\right] \tag{26}$$

and solving for t'

DISTRIBUTION STATEMENT A. Approved for public release. Distribution is unlimited.

$$t' \approx \frac{\left[t - \frac{R}{c} + \frac{\hat{\mathbf{s}}\cdot\mathbf{r}_p(0)}{c}\right]}{\left[1 - \frac{\hat{\mathbf{s}}\cdot\mathbf{v}}{c}\right]}. \tag{27}$$

Now the phase angle of $\mathbf{E}_S(\mathbf{r}, t)$ in equation 24 can be rewritten as

$$\Phi = \mathbf{k}_i \cdot \mathbf{r}_p(t') - \omega_i t' \approx \mathbf{k}_i \cdot \mathbf{r}_p(0) + \mathbf{k}_i \cdot \mathbf{v}t' - \omega_i t' \tag{28}$$

and expanded in terms of t [17] as

$$\begin{aligned}\mathbf{k}_i \cdot \mathbf{r}_p(t') - \omega_i t' &= \mathbf{k}_i \cdot \mathbf{r}_p(0) + \left[k_i(\hat{\mathbf{i}}\cdot\mathbf{v}) - \omega_i\right]\frac{\left[t - \frac{R}{c} + \frac{\hat{\mathbf{s}}\cdot\mathbf{r}_p(0)}{c}\right]}{\left[1 - \frac{\hat{\mathbf{s}}\cdot\mathbf{v}}{c}\right]} \\ &= k_i R\left[\frac{1 - \hat{\mathbf{i}}\cdot\mathbf{v}/c}{1 - \hat{\mathbf{s}}\cdot\mathbf{v}/c}\right] - \omega_i\left[\frac{1 - \hat{\mathbf{i}}\cdot\mathbf{v}/c}{1 - \hat{\mathbf{s}}\cdot\mathbf{v}/c}\right]t - k_i\hat{\mathbf{s}}\cdot\mathbf{r}_p(0)\left[\frac{1 - \hat{\mathbf{i}}\cdot\mathbf{v}/c}{1 - \hat{\mathbf{s}}\cdot\mathbf{v}/c}\right] + \mathbf{k}_i\cdot\mathbf{r}_p(0).\end{aligned} \tag{29}$$

Now the double Doppler shifting relationships between scattered and incident wave numbers and frequencies can be expressed as

$$k_s = k_i\left[\frac{1 - \hat{\mathbf{i}}\cdot\mathbf{v}/c}{1 - \hat{\mathbf{s}}\cdot\mathbf{v}/c}\right] = k_i\left[\frac{1 - v_i/c}{1 - v_s/c}\right] \tag{30}$$

and

$$\omega_s = \omega_i\left[\frac{1 - \hat{\mathbf{i}}\cdot\mathbf{v}/c}{1 - \hat{\mathbf{s}}\cdot\mathbf{v}/c}\right] = \omega_i\left[\frac{1 - v_i/c}{1 - v_s/c}\right]. \tag{31}$$

This allows equation 29 and the phase term to be greatly simplified in terms of scattered parameters as

$$\mathbf{k}_i \cdot \mathbf{r}_p(t') - \omega_i t' = k_s R - \omega_s t - \mathbf{k}\cdot\mathbf{r}_p(0). \tag{32}$$

The Doppler frequency relationship in equation 31 can also be manipulated to derive the Doppler shift as

$$\omega_s(1 - \hat{\mathbf{s}}\cdot\mathbf{v}/c) = (1 - \hat{\mathbf{i}}\cdot\mathbf{v}/c)\omega_i$$

and

$$\omega_s - \omega_i = \omega_s/c(\hat{\mathbf{s}}\cdot\mathbf{v}) - \omega_i/c(\hat{\mathbf{i}}\cdot\mathbf{v}) = \mathbf{k}_s\cdot\mathbf{v} - \mathbf{k}_i\cdot\mathbf{v} \tag{33}$$

which proves the Doppler shift relation given previously in equation 19 as

$$\Delta\omega = \omega_s - \omega_i = \mathbf{k}\cdot\mathbf{v} \tag{34}$$

DISTRIBUTION STATEMENT A. Approved for public release. Distribution is unlimited.

where $\mathbf{k} = \mathbf{k}_s - \mathbf{k}_i$. Finally by combining equations 24 and 32, the scattered electric field can be rewritten in terms of scattering parameters as

$$\mathbf{E}_s = \frac{r_e}{R}\left[\hat{\mathbf{s}} \times (\hat{\mathbf{s}} \times \mathbf{E}_{i0})\right] \cos\left(k_s R - \omega_s t - \mathbf{k} \cdot \mathbf{r}_p(0)\right). \tag{35}$$

The instantaneous energy flux of the scattered radiation is given by the Poynting vector in units of W/m^2 as

$$\mathbf{S} = c\varepsilon_o |\mathbf{E}_s|^2 \, \hat{\mathbf{s}} \tag{36}$$

which means the instantaneous power radiated per unit solid angle [16] in units of W/sr is

$$\frac{dP}{d\Omega} = R^2 c\varepsilon_o |\mathbf{E}_s|^2. \tag{37}$$

An interesting behavior emerges due to the $|\mathbf{E}_s|^2$ term in equation 37 when the scatter power radiated per solid angle from all electrons is considered [18, 19]. This $|\mathbf{E}_s|^2$ term can be expressed as a sum of the scattered field interactions between each pair of electrons, summing over all electron pairs indexed by j and l. This results in a sum of the square of each electron's individual scattered field, as well as cross terms representing collective interaction.

$$\begin{aligned}
|\mathbf{E}_s|^2 &= \sum_j^N \mathbf{E}_{s,j} \cdot \sum_l^N \mathbf{E}_{s,l}^* \\
&= \sum_j^N |\mathbf{E}_{s,j}|^2 + \sum_j^N \sum_{l \neq j}^N \mathbf{E}_{s,j} \cdot \mathbf{E}_{s,l}^* \\
&\approx \left(\frac{r_e^2}{R^2}\left[\hat{\mathbf{s}} \times (\hat{\mathbf{s}} \times \mathbf{E}_{i0})\right]^2\right) \\
&\times \underbrace{\left(\underbrace{\sum_j^N |\cos(\Phi_j)|^2}_{\text{Non-collective}} + \sum_j^N \sum_{l \neq j}^N \frac{1}{2}\left[\cos(\Phi_j + \Phi_l) + \cos(\Phi_j - \Phi_l)\right]\right)}_{\text{Collective}}
\end{aligned} \tag{38}$$

where the sum of the scattered radiation phases of the electron pairs, $\Phi_j + \Phi_l = 2k_s R - 2\omega_s t - \mathbf{k} \cdot [\mathbf{r}_j(0) + \mathbf{r}_l(0)]$, depend on both time and position of electron pairs, but the phase difference, $\Phi_j - \Phi_l = \mathbf{k} \cdot [\mathbf{r}_j(0) - \mathbf{r}_l(0)]$, depends only on electron pair positions. Under assumption of time averaging and combining this with equation 37, the divergent behavior between collective and non-collective regimes can be better understood as

DISTRIBUTION STATEMENT A. Approved for public release. Distribution is unlimited.

$$\left\langle \frac{dP}{d\Omega} \right\rangle = c\varepsilon_o \left(\frac{r_e^2}{2} \left[\hat{\mathbf{s}} \times (\hat{\mathbf{s}} \times \mathbf{E}_{i0}) \right]^2 \right) \left(\sum_j^N 1 + \sum_j^N \sum_{l \neq j}^N \langle \cos\left(\mathbf{k} \cdot [\mathbf{r}_j(0) - \mathbf{r}_l(0)] \right) \rangle \right)$$
$$= c\varepsilon_o N \left(\frac{r_e^2}{2} \left[\hat{\mathbf{s}} \times (\hat{\mathbf{s}} \times \mathbf{E}_{i0}) \right]^2 \right) \Big(\underbrace{\underbrace{1}_{\text{Non-collective}} + (N-1) \langle \cos\left(\mathbf{k} \cdot (\mathbf{r}_j(0) - \mathbf{r}_l(0)) \right) \rangle_{j \neq l}}_{\text{Collective}} \Big) \tag{39}$$

where the term $\langle \cos\left(\mathbf{k} \cdot (\mathbf{r}_j(0) - \mathbf{r}_l(0)) \right) \rangle_{j \neq l}$ represents both the time and ensemble averaged effects of interactions between electrons and will need to be discussed separately for the non-collective and collective cases.

Under non-collective scattering behavior, positions of each electron pair are random. This means in a bulk distribution of electrons, for every electron in a position to produce scatter that interacts constructively with another scatter photon, there is another electron positioned to interact destructively. This causes the average of the cosine term over all pairs of electrons to be zero, and only the first term, N, remains to be multiplied by the left hand side equation 39. This simplifies the equation to only depend on the behavior of each individual particle.

Under collective scattering behavior, on the other hand, certain scattered wavelengths will be enhanced or diminished based on the pattern in the structured (non-random) positions of the electrons according to the cosine term. Because of this, the second term in equation 39 does not go to zero and both terms must be used to calculate the scatter power. In either regime, it is found that only the spectral density function is affected, and in the collective case the interference pattern actually causes $S(\Delta\lambda)$ to no longer be normalized to 1.

In either case, any phenomena that causes changes in the profile of wavelengths can be combined into the spectral density function as

$$\left\langle \frac{dP(\Delta\lambda)}{d\Omega} \right\rangle = c\varepsilon_o N \left(\frac{r_e^2}{2} \left[\hat{\mathbf{s}} \times (\hat{\mathbf{s}} \times \mathbf{E}_{i0}) \right]^2 \right) S(\Delta\lambda) \tag{40}$$

where $S(\Delta\lambda)$ is time and ensemble averaged.

In the case of non-collective scattering, the spectral profile is defined by Doppler broadening, while collective scattering spectra will show both Doppler broadening as well as a contribution from the collective cross terms as shown in equation 39.

The Thomson scatter power, P_T, collected by a detector can also be derived by multiplying the scatter power radiated per solid angle by the small solid angle of detection, $\Delta\Omega$, and expressing N as $n_e AL$ to give

$$P_T(\Delta\lambda) = \Delta\Omega \left\langle \frac{dP(\Delta\lambda)}{d\Omega} \right\rangle = n_e AL \Delta\Omega \frac{1}{2} c\varepsilon_o r_e^2 \left[\hat{\mathbf{s}} \times (\hat{\mathbf{s}} \times \mathbf{E}_{i0}) \right]^2 S(\Delta\lambda). \tag{41}$$

As illustrated in Figure 8, the angle θ is defined between incident and scattered wave vectors, $\mathbf{k}_i$ and $\mathbf{k}_s$, while the angle φ is between the polarization field and the scattered wave vector, $\mathbf{E}_{i0}$ and

DISTRIBUTION STATEMENT A. Approved for public release. Distribution is unlimited.

$\mathbf{k}_s$. The squared factor in brackets in equation 41 has been derived by Jackson to be $[\hat{\mathbf{s}} \times (\hat{\mathbf{s}} \times \mathbf{E}_{i0})]^2 = [E_{i0}]^2 (1-\sin^2\theta\cos^2\varphi)$ which makes the scatter power

$$P_T(\Delta\lambda) = n_e AL\Delta\Omega \frac{1}{2} c\varepsilon_o r_e^2 [E_{i0}]^2 (1 - \sin^2\theta\cos^2\phi) S(\Delta\lambda). \tag{42}$$

Now substituting the incident laser irradiance as $P_i/A = 1/2\varepsilon_o c [E_{i0}]^2$ gives

$$P_T(\Delta\lambda) = n_e L\Delta\Omega P_i r_e^2 (1 - \sin^2\theta\cos^2\phi) S(\Delta\lambda) \tag{43}$$

and including the previously defined constant for a given laser and detection system, $C = LP_i\Delta\Omega$, results in

$$P_T(\Delta\lambda) = C n_e r_e^2 (1 - \sin^2\theta\cos^2\phi) S(\Delta\lambda). \tag{44}$$

Comparing this wavelength dependent Thomson scattering formula to the earlier expression derived for general scattering in equation 10, the differential cross section for Thomson scattering can be deduced as

$$\frac{d\sigma}{d\Omega} = r_e^2 (1 - \sin^2\theta\cos^2\phi). \tag{45}$$

For the experimental configuration in this work, the scatter was collected in a perpendicular direction to the incident laser so that $\theta = 90^o$ resulting in

$$P_T(\Delta\lambda) = C r_e^2 n_e (1 - \cos^2\phi) S(\Delta\lambda). \tag{46}$$

The laser polarization in these experiments was tunable from $\varphi = 90^o$ to $\varphi = 0^o$, which would result in a range of scatter power from $P_T(\Delta\lambda) = Cr^2 n_e S(\Delta\lambda)$ to $P_T(\Delta\lambda) = 0$, respectively. The tunable polarization angle provided a convenient method to record a background signal at $\varphi = 0^o$, while a maximum signal would be recorded at $\varphi = 90^o$. Thus, when configured for maximum Thomson signal with $\theta = 90^o$ and $\varphi = 90^o$, the Thomson scattering power as a function of wavelength will be

$$P_T(\Delta\lambda) = C r_e^2 n_e S(\Delta\lambda) \tag{47}$$

with the spectral shape defined by $S(\Delta\lambda)$, which is described differently for each Thomson scattering regime in the following sections.

As mentioned in the introduction, Thomson scattering between incident radiation and electrons may exhibit collective or non-collective behavior depending on the length scale of the electromagnetic interaction compared to the Debye length, where generally non-collective behavior occurs when $\lambda_i \ll \lambda_D$ and collective when $\lambda_i \gg \lambda_D$. To better distinguish these collective and non-collective scattering modes, the unitless scattering parameter α is introduced as

DISTRIBUTION STATEMENT A. Approved for public release. Distribution is unlimited.

$$\alpha = \frac{1}{k\lambda_D} = \frac{\lambda_i}{2\sqrt{2}\pi\lambda_D}. \tag{48}$$

A more accurate assignment of non-collective or collective scattering is that $\alpha < 1$ tends toward a non-collective scattering behavior, while $\alpha > 1$, tends toward a collective scattering profile. As this description of Thomson scattering extends to consider a system of many electrons, the derivations will differ when assuming non-collective scattering or collective scatter and thus will be presented in two separate sub-sections.

3.2.3 Non-Collective Thomson Scattering

For non-collective Thomson scattering, the profile of the spectral density function is caused solely by the double Doppler broadening. For a Maxwellian distribution of electron velocities, according to the derivation by Sheffield et al. [18], the spectral density function takes on a Gaussian shape as

$$S(\Delta\lambda) = \frac{1}{\Delta\lambda_{1/e}\sqrt{\pi}} \exp\left[-\left(\frac{\lambda_s - \lambda_i}{\Delta\lambda_{1/e}}\right)^2\right] \tag{49}$$

where the parameter $\Delta\lambda_{1/e}$ is the $1/e$ half-width of the Gaussian distribution in units of length and is defined for non-collective Thomson scattering a

$$\Delta\lambda_{1/e} = \lambda_i\sqrt{\frac{2k_BT_e}{m_ec^2}}. \tag{50}$$

By measuring the $1/e$ half-width of the Gaussian shape of the spectrum, the average electron temperature can be calculated as

$$T_e = \frac{m_ec^2}{4k_B}\left(\frac{\Delta\lambda_{1/e}}{\lambda_i}\right)^2. \tag{51}$$

In this work, with a $\lambda_i = 532$ nm source laser and a measurement of $\Delta\lambda_{1/e}$ in nm, the electron temperature in units of eV can be calculated as $T_e = 0.452\ \Delta\lambda_{1/e}^2\ [eV]$

The electron density for non-collective scattering can be found once the peak and width of the spectrum is determined by a Gaussian fit, which then provides values for P_{Tmax} and $S(0) = 1/(\Delta\lambda_{1/e}\sqrt{\pi})$. From equation 47, the electron density within a non-collective scatter region can be expressed as

$$n_e = \frac{P_{Tmax}\ \Delta\lambda_{1/e}\sqrt{\pi}}{Cr_e^2}. \tag{52}$$

In this work, the value C was substituted with Raman scattering parameters through a Raman scattering spectral analysis and calibration under the same laser and detector conditions using

DISTRIBUTION STATEMENT A. Approved for public release. Distribution is unlimited.

equation 16. The absolute value of n_e could then be determined from the best fit of the relationship

$$n_e P_R(\Delta\lambda) = \frac{P_{Tmax}\Delta\lambda_{1/e}\sqrt{\pi}}{r_e^2}\left(\sum_{J'=J\pm2} n_J \frac{d\sigma_{J\to J'}}{d\Omega} S(\Delta\lambda - \lambda_{J\to J'})\right). \tag{53}$$

In this process, the electron density n_e acts as a variable to provide a least squares fit when multiplied by the experimental Raman spectrum and fit with the combined experimental and theoretical calibration terms on the right hand side of the equation.

3.2.4 Collective Thomson Scattering

In a plasma with high electron density, even when the velocity of the electrons are still assumed to have a Maxwellian distribution, the collective behavior of the charges interacting with the incident radiation results in a fairly complex spectral scattering distribution. One reason for this behavior is the plasma oscillations which cause changes in density of the plasma across the **k** vector. First published by Salpeter in 1960 [20], the determination of the spectral density function from these oscillations in collective scattering becomes much more complex than for non-collective scattering.

Reciting the full derivation concerning collective Thomson scattering would not be of particular value here, so the result of the derivation in Chapter 5 of Sheffield et al. [18], is simply given here for the electron component of the spectral density function as

$$S(x_e) \approx \frac{2\sqrt{\pi}}{ka}\frac{exp(-x_e^2)}{[(1+\alpha^2 \mathrm{Rw}(x_e))^2 + (\alpha^2 \mathrm{Iw}(x_e))^2]} \tag{54}$$

where $a = \sqrt{2k_B T_e/m_e}$ is the mean thermal speed of the electrons, $x_e = \Delta\omega/(ka)$ is a convenient dimensionless frequency parameter. By using p, a dimensionless dummy variable that is integrated out when calculating Rw, the real and imaginary parts of the plasma dispersion function are, respectively,

$$\mathrm{Rw}(x_e) = 1 - 2x_e exp(-x_e^2)\int_0^{x_e} exp(p^2)dp$$
$$\mathrm{Iw}(x_e) = \sqrt{\pi}x_e exp(-x_e^2)$$

Upon inspection of equation 54, the magnitude of the parameter α can be seen to drive the mathematical shape of S between collective and non-collective regimes. As α increases, the Rw(x_e) and Iw(x_e) terms in the denominator which create the saddle-like shape of the spectrum become more significant while the Gaussian term in the numerator becomes less of an influence.

Unlike non-collective scattering, this collective spectral density function cannot be normalized to 1 due to certain spectral features lost to collective scatter interference. Thus, calibrating the Thomson spectrum along with a Raman spectrum becomes overly challenging. Fortunately, the spectral density function in the collective regime in equation 54 has a distinct shape that depends on both average electron temperature and electron density so that these parameters can be found through a direct fit.

DISTRIBUTION STATEMENT A. Approved for public release. Distribution is unlimited.

4. Previous Work

Many types of plasmas have been researched with potential benefits across a variety of fields. These plasmas are generally characterized by their charge density as well as temperature but also may be distinguished by their excitation source. In laboratory science, two main groups of plasmas exist; high-temperature or fusion plasmas and low-temperature plasmas or gas discharges, with the work in this thesis focusing on the latter. According to Bogaerts et al. important types of low temperature plasmas include direct current (dc) discharges, radio frequency (rf) discharges, pulsed glow discharges, atmospheric pressure glow discharges, dielectric barrier discharges, microwave induced plasma, expanding plasma jets, and dusty plasmas [21]. Different gas mediums have been investigated such as creating a discharge in pure argon environments [22, 23], in gas mixtures with helium [24, 25], and in open lab air environments [26, 27] as explored in this thesis.

A glow discharge is characterized as a partially ionized gas, where a relatively low current at high voltage sustains the level of ionization in the plasma, but does not heat the gas significantly [28]. At atmospheric pressure, glow discharges in air easily transition into spark discharges, where an increase in the conduction of the plasma causes the voltage to drop and the current to rise [29]. The higher current causes joule heating that significantly increases the gas temperature, which is problematic for applications sensitive to high temperature.

Repetitively pulse high voltage nanosecond discharges in air are being investigated in this work. Applying the high voltage over a limited timescale similar to the discharge generation time has been shown to produce higher number densities of reactive species than classical discharges while maintaining moderate gas temperatures [30]. The comparatively low energy budget of the short duration pulses also promotes a very efficient discharge system [31]. Despite numerous experimental studies on the effect of repetitive nanosecond pulses on the generation of energetic species and their resulting kinetics leading to ignition [32, 33, 34, 35], very little is known about the electron density and energy distribution during and between the nanosecond pulse discharges.

Various methods have been used to measure parameters of plasma [36]. Langmuir probes have been used to find electron density measurements [37], but the intrusive nature of the metal probe effects the plasma and may alter the same parameters that are being measured. Optical emission spectroscopy is non-intrusive and typically easy to implement, but the underlying collisional radiative models are often very complex and a number of assumptions must be made to unambiguously derive plasma parameters [38].

Laser light scattering, including Rayleigh, Raman, and Thomson scattering, has been found to be relatively non-intrusive and provide direct measurement of plasma properties, although experiments can involve expensive equipment, painstaking alignment, and long measurement times. Rayleigh elastic scattering from neutral molecules was theorized and applied over a century ago by Tyndall, Rayleigh, Schuster, and others to explain the blue tint of the spectrum of Earth's daytime sky [39]. Rayleigh scattering has more recently allowed researchers to determine densities of scattering particles in plasmas using lasers [40, 41] and microwave sources [42, 43].

Raman scattering, on the other hand, is inelastic in nature and shifts the scattered radiation wavelength according to a molecule's rotational and vibrational structure. This allows for an analysis of rotational and vibrational energy distribution within a plasma using laser light [44].

DISTRIBUTION STATEMENT A. Approved for public release. Distribution is unlimited.

When Raman shifted wavelengths are overlapped with Thomson scattering features in air, the well known molecular spectroscopic parameters of air have made the Raman profile a useful calibration method [15].

Thomson scattering theory involving light scattering off electrons was used in the mid-1900s to explain solar corona observations [45] and measure the electron density in the solar corona [46]. The advent of the laser in the 1960s along with an interest in high temperature plasmas showed that laser Thomson scattering was effective in determining electron density and temperature in these dense plasmas [47]. Laser Thomson scattering was found to be very effective in the analysis of high temperature fusion plasma experimental systems such as the Tokamak [48]. Thomson scattering has more recently been applied to the analysis of low temperature jets [49, 50] although the lower electron density presents a challenge for resolution.

Laser scattering measurements techniques are not without their own drawbacks. The laser required to generate scattering can impart some of its energy to the plasma as it passes through. This electron heating effect has the potential to raise the temperature of the plasma [51] and in some cases can increase electron density through additional ionization [52]. These effects must be monitored in any experimental effort and taken into account if electron heating or ionization is found to have a non-negligible effect.

DISTRIBUTION STATEMENT A. Approved for public release. Distribution is unlimited.

5. Experimental

The experimental portion of this work used laser Thomson scattering to measure both the electron density and temperature at various times between repetitive nanosecond pulse discharges in air. A high voltage repetitive nanosecond pulse source created bursts of discharges in air with an adjustable repetition rate up to 200 kHz between a pin-to-pin electrode gap. Density and temperature measurements were derived from the spectral distributions of Thomson scattered light as 532 nm pulsed laser light passed perpendicularly through the interelectrode axis, as shown in Figure 10, and scatter was dispersed using a TGS and recorded with an intensified CCD camera. A diagram of the overall experimental setup is laid out in Figure 11, with each element of the experiment discussed in detail in the following sections.

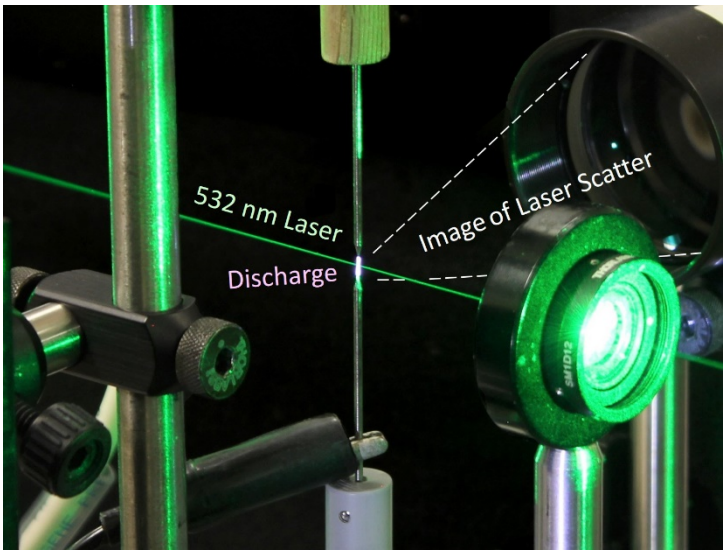

Figure 10: Photograph of laser passing through a vertical nanosecond pulse discharge creating scattered light that is collected by a lens.

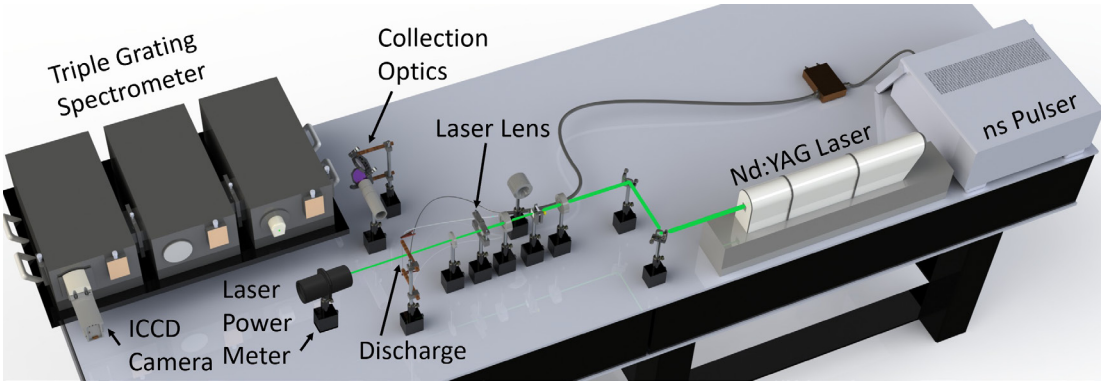

Figure 11: A diagram of the experimental setup

5.1 Nanosecond Pulsed Discharge

A Transient Plasma Systems (TPS) nanosecond repetitively pulsed power supply was used to apply bursts of repetitive pulses of 15 kV with a 10 ns pulse duration. The nanosecond high voltage pulses were delivered to a pin-to-pin electrode configuration. The nanosecond repetitively pulsed discharges (NRPDs) created between the electrodes were generated by a simple circuit, consisting of the custom built pulsed power supply a resistor, and the two pin gap. The 12 Ω resistor in series with the discharge load prevents an accidental short circuit from

DISTRIBUTION STATEMENT A. Approved for public release. Distribution is unlimited.

damaging the power supply while limiting any interference with normal nanosecond pulse discharge operation. Previous experiments with the identical pulser and electrode configuration found that a single pulse deposited approximately 8 mJ into the electrode gap [53].

Two 1.6 mm diameter lanthanated tungsten electrodes sharpened to a conical 20° cone angle were placed 2 mm apart vertically to form the discharge in open air. The pins consist of two tungsten rods separated by a 2 mm gap exposed to an open lab environment.

Since the medium for the plasma is typical lab air, the standard room temperatures, densities, and gas mixtures were assumed prior to the first pulse of each burst. The pins and gap were the components most susceptible to day-to-day changes in the experiment. After many discharges across several days, the pins would wear down and require resharpening. Variations in the separations in the gap were found to have an effect on densities and temperatures within the plasma, so the accuracy in the set up was critical. On top of this, environmental changes in the air could also contribute to changes in plasma parameters. To reduce the effect of environmental changes, each data set for a given burst condition was collected within its own day.

The power supply and timing system were capable of a large variety of burst modes. In this thesis, three scenarios were examined where the discharge burst consisted of A) one single pulse, B) a burst of two pulses at a repetition rate of 100 Hz, or C) a burst of four pulses at a repetition rate of 200 Hz. In order to accumulate data and improve image resolution, the bursts were repeated at a relatively slow rate of 10 Hz which allowed the discharge region to fully recover between bursts.

5.2 Pulsed Laser

A Quantel Brilliant pulsed Nd:YAG laser with a second harmonic generator crystal produced 532 nm laser light with 7 mJ of energy per pulse. The beam propagated horizontally along the optical table and was focused through the center of the vertical discharge

to perform the Thomson scattering, as shown in Figures 10 and 11. For improved control over the polarization and power of the laser light incident on the plasma, the laser was first passed through a small optical system of waveplates and a beam cube as shown in Figure 12. The first waveplate adjusted the polarization of the beam passing through a beam cube. The beam cube redirected a certain fraction of the laser toward a beam dump depending on the first waveplate setting and allowed the remaining light to continue through. Immediately after the beam cube, the laser passed through a second waveplate to set its final polarization. By adjusting the polarization of these two wave- plates, the operator was able to control both the amount of power and the polarization of the incident light.

DISTRIBUTION STATEMENT A. Approved for public release. Distribution is unlimited.

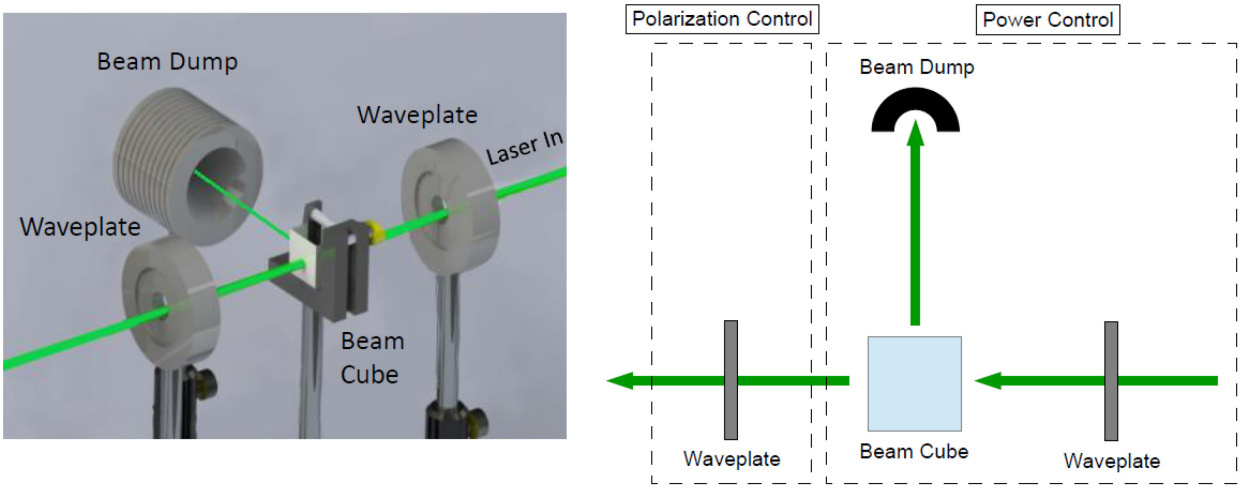

Figure 12: Graphic view and a diagram of the polarization and power control optics in the laser path prior to the scattering region

Once power and polarization were set, the laser was focused using a lens with a focal length of 300 mm. The beam was tightest within the discharge region of interest with a beam width of about 200 μm. Although the width of the beam slightly changed through space, across the short length observed by the spectrometer the width was assumed constant. This beam approximates the cylinder in Figure 6 in the cross section discussion in Section 3.2. The laser passes through the discharge volume with a small fraction of the light scattered, a small fraction absorbed by the plasma, and the remainder continuing through to a power meter. Since such a small portion of light is scattered/absorbed under the normal circumstances, the laser power recorded by the power meter is nearly the same as the laser power entering the plasma.

5.3 Collection Optics

The scattered light collected is very weak since the particles have such a small cross section with which to interact with the incident laser. To maximize the signal, scattered light is collected at right angles to both the discharge axis and the laser (corresponding to $\theta = 90°$, $\varphi = 90°$ in equation 43). The scatter is initially collected near the discharge region with a lens 5 cm in diameter with a 100 mm focal length. The light is sent through a pair of periscoped mirrors to rotate the image which is then projected with a 5 cm diameter 250 mm focal length lens onto the slits of the spectrometer.

DISTRIBUTION STATEMENT A. Approved for public release. Distribution is unlimited.

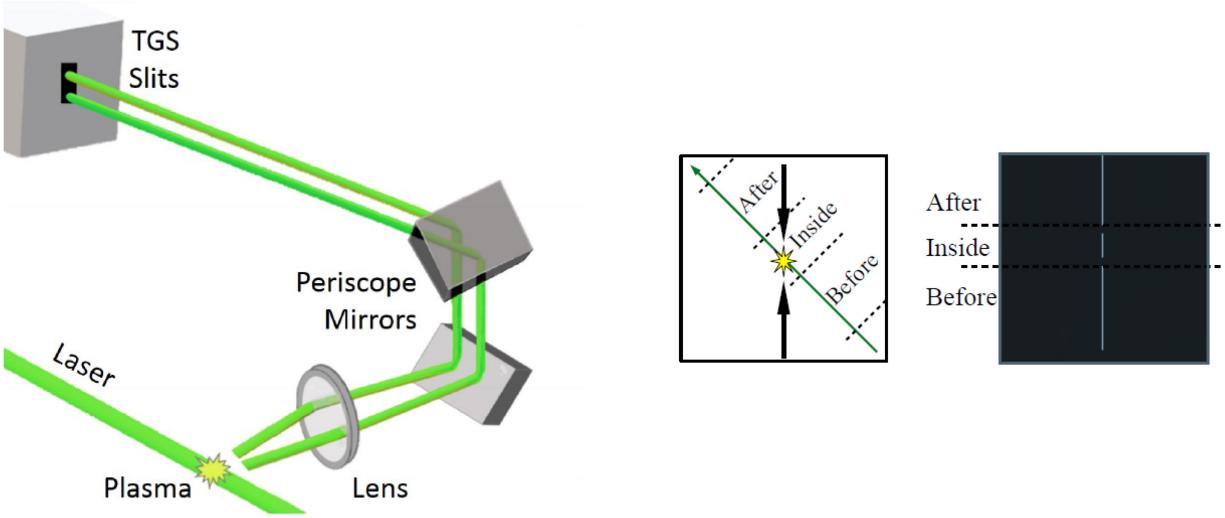

Figure 13: Laser scatter near the plasma is collected and rotated by periscoping mirrors so that the image is vertical on slits (left drawing)

The three vertical regions on the slits represent (bottom to top on right image): before laser passes through plasma, laser inside plasma, and after laser passes through plasma.

In order to disperse and analyze the scattered wavelengths, the collected light was directed with a periscope onto the slits of the TGS so that the line of scattered aligned with the slits allowing for spatial resolution of the image along the laser path. As shown in Figure 13, the line of scattered light imaged onto the slits represents, bottom to top, the light scattered before entering the plasma, while inside the plasma, and after exiting the plasma.

5.4 Triple Grating Spectrometer

The TGS has a dual purpose by both dispersing the wavelengths of scattered light and removing unwanted bands of wavelengths. The TGS consists of three separate spectrometers each containing a diffraction grating. As shown in Figure 14, light enters though slits on one side of the TGS and is passed through each spectrometer sequentially. The first two spectrometers combine to remove a band of wavelengths based on the position and width of a mask positioned between spectrometers 1 and 2. The third spectrometer then disperses the light to give a final spectrum with the unwanted wavelength band removed. The resulting image from the TGS is recorded on a Princeton Instrument gated ICCD camera.

As discussed previously, Rayleigh scattering is very intense compared to either Thomson or Raman scattering and does not shift from the wavelength of the incident laser light. Therefore, a primary function of the TGS is to introduce a mask that removes the Rayleigh scattered light by blocking a small band of wavelengths centered on the laser wavelength and allowing the weaker side bands of Raman and Thomson scattering to be observed by the camera without being overwhelmed by the Rayleigh scattering.

DISTRIBUTION STATEMENT A. Approved for public release. Distribution is unlimited.

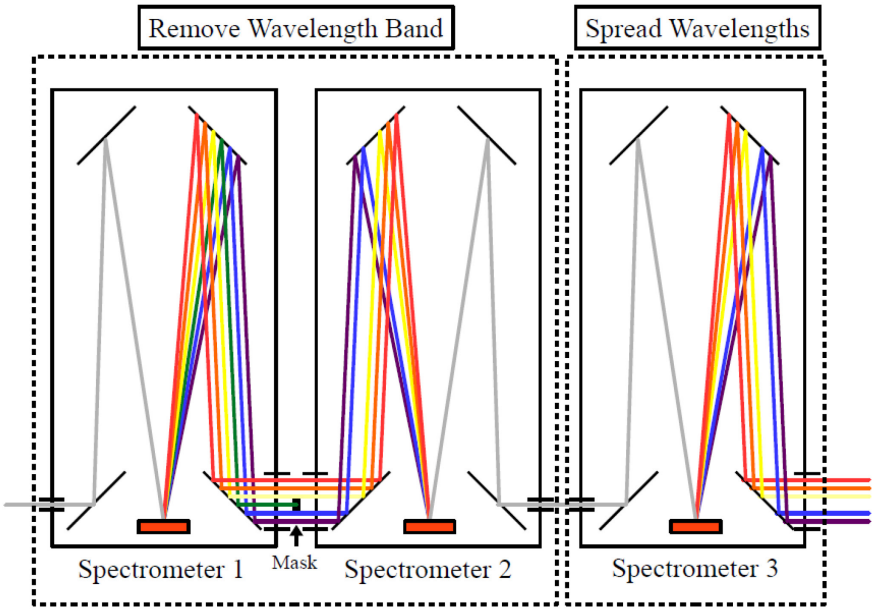

Figure 14: A simplified top-down diagram of the TGS

Light enters from an opening on the rightmost box and exits the leftmost box. Spreading is exaggerated to better visualize the removal of specific wavelengths of light.

The slit at the entrance of the first spectrometer is set to 350 μm, which defines the resolution of the spectral dispersion but also limits the total light throughput. A series of mirrors and a diffraction grating within the first spectrometer disperses the light horizontally before passing this light toward the second spectrometer. Between the first and second spectrometer, a 1 mm mask physically blocks out the range of wavelengths located near 532 nm before entering the second spectrometer. This step may appear to be enough to completely remove the unwanted wavelengths, but the following describes the essential functions of the second and third spectrometer in assuring the complete removal of the unwanted wavelength band.

Each wavelength that is dispersed by first spectrometer will experience some broadening due to the entrance slits and diffraction grating. Although this slight broadening is not a problem for many spectral applications, the Rayleigh scatter being blocked here is so bright that even the unblocked wings of its broadened profile will corrupt observation of the Raman and Thomson scattering using a single spectrometer. To fix this phenomenon, Figure 15 shows how the diffraction process is reversed in the second spectrometer using the diffraction grating to recombine the spectrum back into, roughly, a single vertical line image. Since the light from the broadened wings of the first diffraction grating are misplaced in the spectrum, these wings do not converge at the same vertical line position as the rest of the scatter. By then passing this reconverged light through the slit of the third spectrometer, with a slit width similar to the first spectrometer, the misplaced light is unable to pass through and this completes the removal of the intense Rayleigh scatter. The third spectrometer then simply disperses the remaining scattered light horizontally which is imaged by the intensified CCD camera.

DISTRIBUTION STATEMENT A. Approved for public release. Distribution is unlimited.

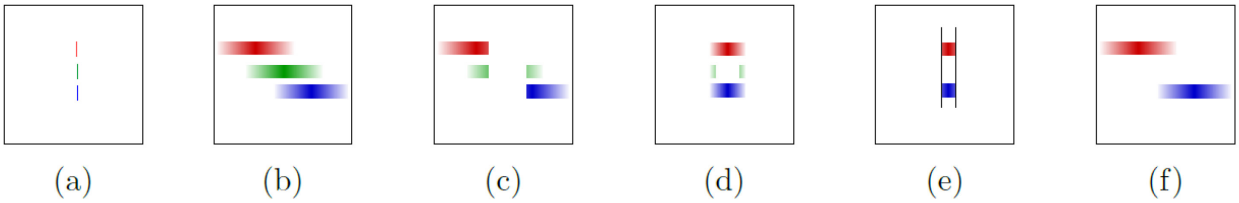

Figure 15: Removal of Rayleigh scatter in TGS

(a) Light of various wavelengths enter slit, (b) the 1st spectrometer disperses light, (c) mask between 1st and 2nd spectrometers removes central green Rayleigh but intense Rayleigh wings remain, (d) the second spectrometer recombines remaining light, (e) slit of the third spectrometer completely eliminates intense wings of central Rayleigh scatter (f) disperses the remaining red and blue shifted light with Rayleigh removed completely.

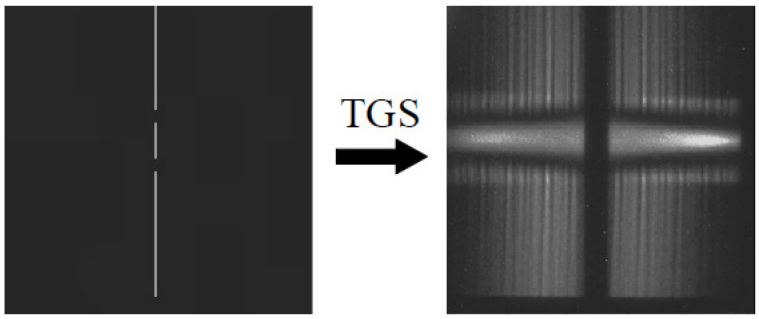

Figure 16: The TGS receives a narrow line of light (rendition on the left) and separates the wavelengths from lowest to highest (example on the right)

Figure 16 shows how the vertical scattering image focused on the input slits of the TGS results in a spatially resolved spectral image at the camera. The dispersed spectral image on the right clearly shows the central vertical Rayleigh scattering feature removed from the spectrum. The spectral pattern on the top and bottom are also clearly different from the horizontally central region. This will be discussed later as being due to the Raman scattering in air dominating the top and bottom, while Thomson scattering in the plasma dominates the horizontal central region of the image.

Although the slits and gratings within the TGS are an additional source of instrument broadening of the final spectrum, it is found that these contributions are negligible compared to the Doppler broadening in the Thomson scattering profile. Since the TGS has a relatively high spectral resolution in dispersing the spectrum the scattered light, convoluting the Doppler broadening with the TGS instrument broadening does not meaningfully change the profile.

5.5 Timing

The timing of the pulsed laser, pulsed discharge, and gated camera were all controlled by a single Stanford digital delay generator. The intensified CCD camera could be digitally gated to only collect light over a short time period, down to about a 2 ns window. It was desired that the gated camera only accumulate an image of the scatter during the laser pulse. The Nd:YAG laser used to produce the scattering is only ‘ON’ for about 7 ns, so the camera gating was set to 10 ns to insure the full laser scatter was capture, but to also minimize any light noise from other events. With such a quick timetable, there were still slight time delays between trigger pulses and actual optical turn on of these devices. This was compensated for, as well as any other signal delay, by adjusting the internal delay time of the camera’s start and calibrating it to capture the maximum scattered light from the laser.

DISTRIBUTION STATEMENT A. Approved for public release. Distribution is unlimited.

The NRPD source, as the name would imply, completely deposited the majority of its energy into the pulse discharge in only about 10 ns. Some ringing effects were observed as some of the voltage pulse bounced or reflected from the pin-to-pin gap, returned to the supply, bounced off the power supply, and returned to the gap. This process repeated with weaker and weaker subsequent reflections. The burst of pulse discharges was typically set by the delay generator to initiate at some given time before the laser and camera, as this work was investigating electron properties between the pulsed discharges.

Akin to flash photography, the image of the scatter was taken at a certain time by flashing the region of interest with the laser and accumulating the scattered light. By delaying when the start of the laser/camera system began, refereed to as τ in Figure 17, a specific time after the initial discharge was initiated can be imaged. In this experiment, the variable delay of the laser and camera after the initial pulse was incremented in steps. For times when plasma properties were changing rapidly, such as immediately following a discharge, the time was incremented in steps of 0.25 μs. For times longer after the discharge the steps were incremented at 1 μs. A simplified timing diagram is shown in Figure 17 for the case of a 4 pulse burst at 200 kHz and the laser and camera probing a certain time after the third pulse.

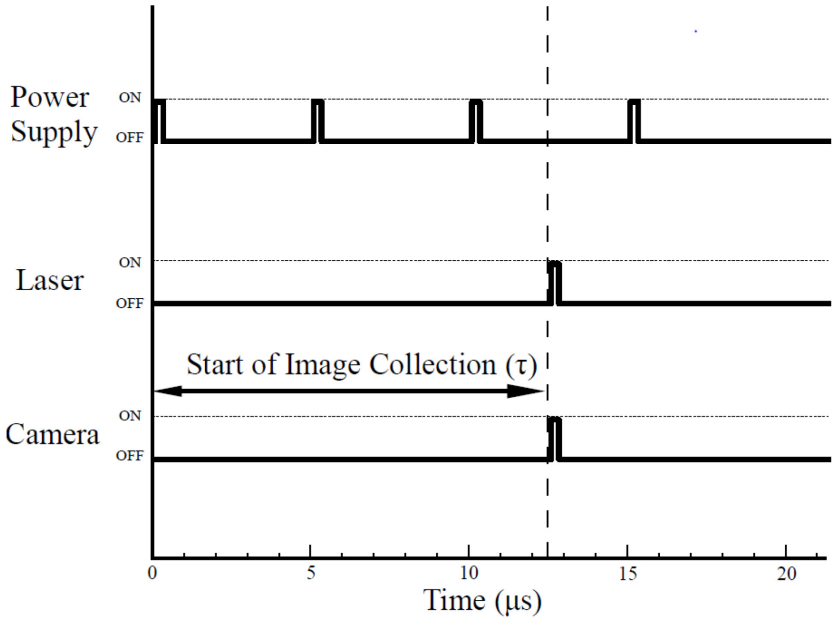

Figure 17: Simplified diagram of the timing with a four-pulse burst at 200 kHz shown as an example. Power supply, laser, and camera pulse durations are exaggerated as they are roughly 10 ns, 7 ns, and 10 ns, respectively.

A single spectral image was not sufficient to accurately measure the plasma parameters due to the weak signal of Thomson and Raman scattering, therefore 5000 frames were accumulated into a single output image for each time after the initial discharge. For every shot of the accumulation, the timing process is repeated; creating the discharge burst, waiting a variable amount of time τ , then flashing the area of interest to record the scatter spectral image. The process repeats at 10 Hz, which allows plenty of time for the discharge region to return to equilibrium with the environment in that 1/10 of a second. On occasion, bright artifacts would be created on the image due to reflection from large particles or electrical effects. To remove these

DISTRIBUTION STATEMENT A. Approved for public release. Distribution is unlimited.

artifacts efficiently, the 5000 accumulations were broken into 10 subimages, each representing 500 accumulations, so that an artifact would only effect a subimage instead of the entire 5000 shot output image. Any bad subimages are removed during the post processing and the remaining good subimages are averaged together into a single output image. If too many subimages were ruined by bright artifacts, then the batch was retaken.

5.6 Post Processing

The x axis of the resulting output images was assigned a very accurate scaling of wavelength by calibrating against the profile found from an image of Raman scattering. Some Raman scattering was typically visible in each output image due to the atmospheric air surrounding the discharge region and the spectral shifts are well known from the theory presenting in Section 3.2.1. An output image of Raman scattering taken without a discharge, though, was used for calibration of the n_e measurement from the Thomson scatter.

Within each output image for the same burst mode and time, the 10 subimages should be roughly identical. Therefore, the sum of the pixel intensities should be roughly the same between each subimage in the same batch unless an artifact is present. By looking at the pixel sum of each subimage and comparing it to the median of the batch, bad subimages are identified to remove if they are above a certain threshold. The remaining good subimages of the batch are averaged into a single output image.

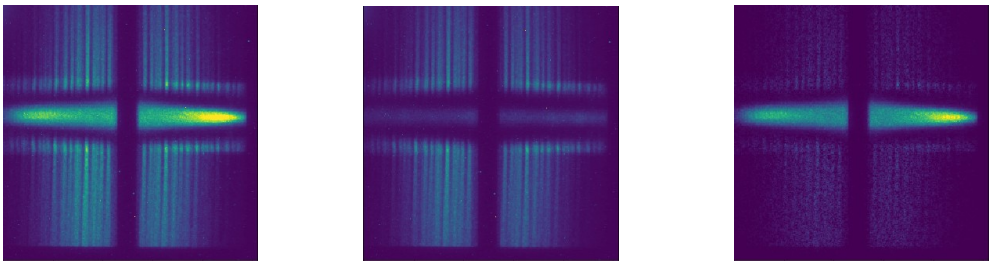

(a) Raw Image (b) Background image (c) Final Image

Figure 18: Processing a Thomson scattering image

(a) The raw image has the (b) background image (c) subtracted from it to create the final image

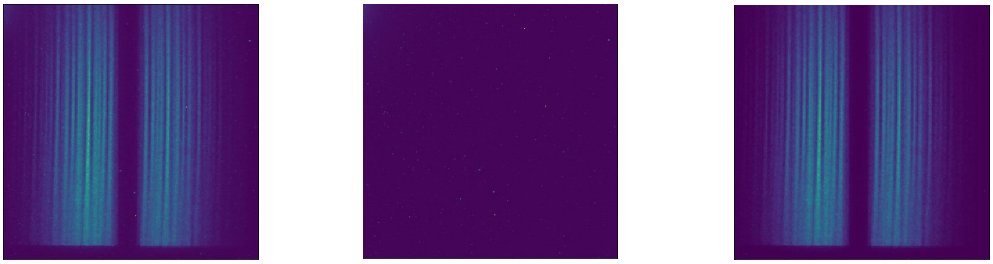

(a) Raw Image (b) Background image (c) Final Image

Figure 19: Processing a Raman scattering image

(a) The raw image (b) has the background image (c) subtracted from it to create the final image.

DISTRIBUTION STATEMENT A. Approved for public release. Distribution is unlimited.

For each image taken, a background image is subtracted from the raw image. For images of Thomson scattering, the waveplate is rotated until there is no Thomson scattered light being directed toward the collector, corresponding to $\theta = 90^\circ$, $\varphi = 0^\circ$ in equation 43.

This image at $\varphi = 0^\circ$ still contains the stray laser light, plasma emission, and other non-Thomson scattering effects, so it is ideal for use as a background image to subtract from the Thomson scattering output image, as demonstrated by the example raw, background, and final images shown in Figure 18b. For the Raman scattering features, the Raman signal is reduced at $\varphi = 0^\circ$, but does not go to zero, so some Raman scattering remains in the background subtracted image, but it is usually spatially separated from the Thomson scatter. When background subtraction is required for the analysis of the Raman scattering itself, then a background image is taken with the discharge and laser off to subtract effects such as stray light and bad pixels, as demonstrated by the example Raman images processed in Figure 19b. Following this procedure, every measurement point of data requires four images to produce: an image containing the Thomson scattering at the desired time, a background image for the Thomson scattering image also at the desired time, an image containing Raman scattering, and a background image for the Raman scattering image.

While Raman scattering is captured in each Thomson scattering image outside of the low density region, the discharges were observed to disturb these areas enough to make them unattractive for electron density calibration. Early on, a shockwave could be seen traveling through each region originating from the center, while repeated pulses were shown to expand the low density region to the borders of the camera. To enhance the accuracy of the calibration, the Raman scattering image used for calibration was taken the same day as the set of Thomson scattering images to be calibrated. Multiple Raman scattering images were also taken throughout the day to monitor any drastic changes.

From the the background subtracted output image for both types of scattering, five pixel rows were vertically binned for analysis of the intensity profiles. As seen in Figure 20, the five rows of pixels (rows between the blue dashed lines) were averaged together into a single trend of intensities.

DISTRIBUTION STATEMENT A. Approved for public release. Distribution is unlimited.

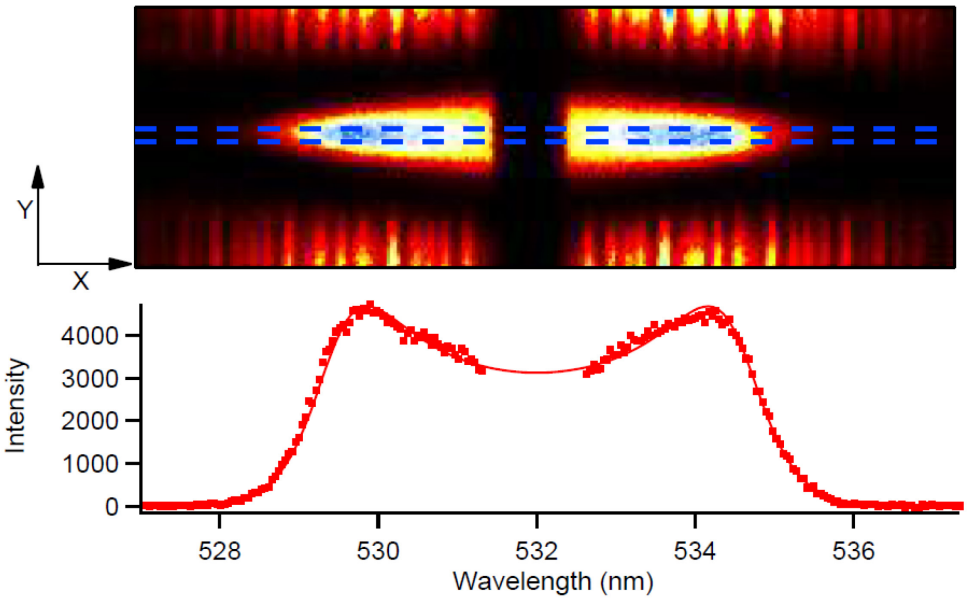

Figure 20: The raw image (top) is binned across five pixels to create a series of points (bottom) at each location

The equations are fit to the data to produce the line.

The camera pixel array was found to contain an intensity bias for some pixel over others, so some correction was require there as well. The light of an attenuated 532 nm laser was shone indirectly onto the slits of the TGS and the image was recorded. By rotating the diffraction gratings in the TGS, the 532 nm light was imaged at various positions on the pixel array of the camera. At each position, the camera recording the trend of intensities. Since the laser was being held at constant power, this change of intensity was representative of the system's light sensitivity bias. This bias was corrected from the final output image by dividing out the bias trend.

For the first step in calibrating the spectral images, equation 11 is fit to a Raman scatter spectrum in air to properly scale the x axis in terms of wavelengths. For both the non- collective and collective regime of Thomson scattering, the same equation 47 for scatter power as a function of wavelength can be applied, but the spectral density function, $S(\Delta\lambda)$, will differ between regimes. Salpeter's spectral density function equation 54 in theory could be applied to both collective and non-collective regimes [20], but since the central 532 nm wavelength is removed from the experimental data by the TGS mask, this dramatically increases the uncertainty for fits using equation 54 when the spectral peak is not recorded, such as with the non-collective Gaussian spectra. Therefore, separate equations are used to fit each regime. The non-collective scattering spectra were fit with a least squares routine to determine the Gaussian 1/e half-width, $\Delta\lambda_{1/e}$, and then by applying equation 51, the electron temperature, T_e, was found. Electron density, n_e was calculated comparing the amplitude of the non-collective spectrum to the calibration constant obtained from the Raman trend in equation 53. For collective scattering, average electron temperature and density measurements were found by directly fitting them as parameters to the profile of the collective scattering trend from equation 54.

DISTRIBUTION STATEMENT A. Approved for public release. Distribution is unlimited.

6. Results

6.1 Time Resolved Electron Temperature and Electron Density

Due to the rapidly changing electron temperatures and densities between 1 μs and 10's of μs after the pulse discharge, the Thomson scatter from the plasma was seen in both the collective and non-collective regimes at different times throughout the experiment. Plotted in Figure 21 are a set of four fitted spectra from the first few μs after the first discharge pulse.

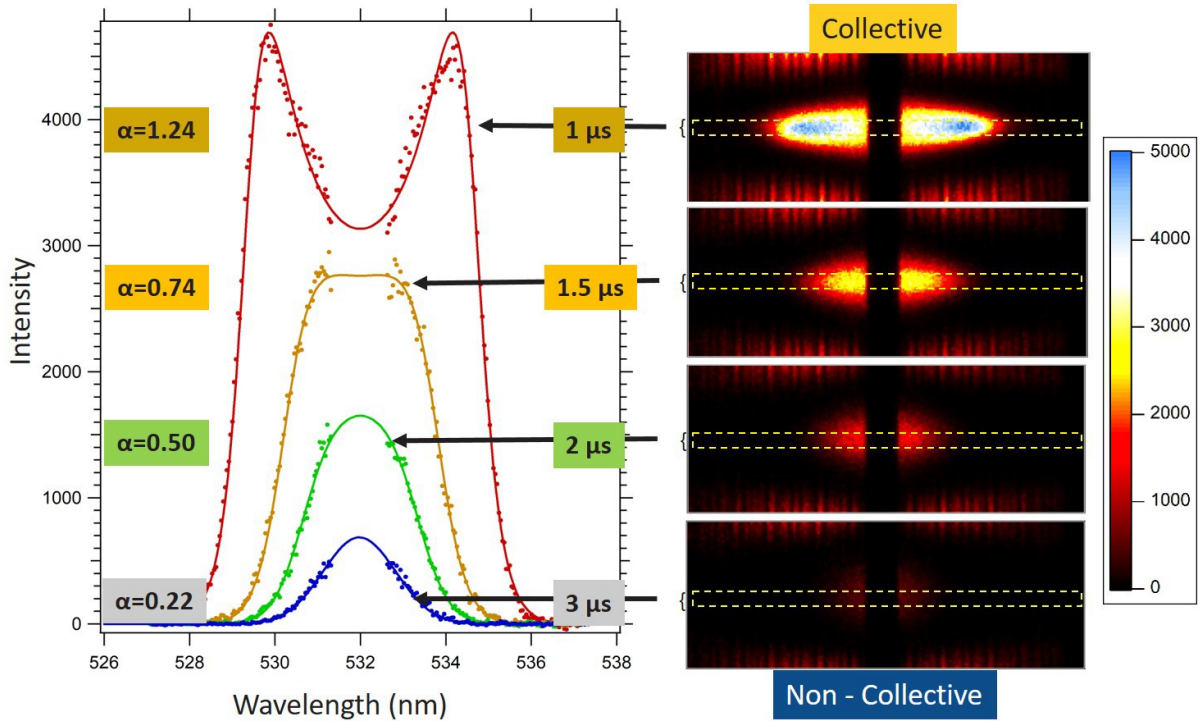

Figure 21: Plots of intensities collected versus wavelength at various times after the initial discharge

The dots represent data collected from the experiment. The lines are the fits for each dataset, with the spectral images shown to the right. The collective fit was used for the first three times (1.0 µs, 1.5 µs, 2.0 µs), while the non-collective fit was used for the last time (3.0 µs). Shown to the left of each graph are the α values calculated from the fit's density and temperature parameters.

The times are relative to the beginning of the first pulse, and show a decrease in signal intensity as time increases, along with a change in spectral shape characteristic of a change from collective to non-collective Thomson scattering behavior.

Prior to 3 μs, each of the three spectra were fit using collective scattering theory, where the shape can be fit with values of n_e and T_e. The best fit α values for each spectrum are also displayed and show a decrease of α with time. For this work, the time dependence of α is mostly due to the change in n_e over time. At 3 μs the spectra in Figure 21 becomes very Gaussian, and unique values of n_e and T_e could not be determined from collective scattering theory. Data points closer to the central wavelength that were blocked by the mask may have allowed further spectral analysis to determine n_e, but were too entangled with the laser Rayleigh scatter. The α value for the 3 μs spectrum as well as those at later times are clearly Gaussian and analyzed using the method outlined previously with n_e and T_e found through non-collective Thomson scattering theory. The α is found to be lower than at earlier times, as expected. The transition from

DISTRIBUTION STATEMENT A. Approved for public release. Distribution is unlimited.

collective to non-collective is evident in Figure 21 where the line shape transformed to a Gaussian while α decreases. The two nodes characteristic of collective scattering merged as time progressed. Although a decrease in temperature would encourage collective behavior, the more rapidly decreasing density becomes the main driving force of determining collective versus non-collective scattering behavior.

Using the timing systems developed in the previous chapter, measurements can be taken of electron temperature and density at various points of time throughout the life of the plasma. The data presented here are the electron density and temperature at various times after the discharge for three burst modes, applying either one pulse, a two-pulse burst, or a four-pulse burst. Electron density is plotted on a logarithmic scale due to the wide range of densities seen throughout the dataset, while electron temperature is plotted linearly.

Typically, the electron density would decrease very quickly in a background of atmospheric air, yet the data here show the density decaying much slower than expected after several microseconds. From the images of Thomson scattering, such as Figures 18 and 20, the lack of Raman scattering in the center following a discharge indicates a low density region forming as the violent discharge sends a shockwave of air outward. This low density region lasts until roughly 20 μs to 25 μs after the final pulse, at which point the air begins to rush back in. Therefore, it is reasonable to assume that the electron recombination and attachment rate would be lower in the lower gas density regions and provide justification for the observation of the electron density remaining relatively high for an extended period of time. This extended existence of remnant electrons has been seen in prior work, although no electron temperature measurements were made [42].

Figures 22a and 22b show plots of electron temperature and electron temperature, respectively, with time after a single pulse discharge.

DISTRIBUTION STATEMENT A. Approved for public release. Distribution is unlimited.

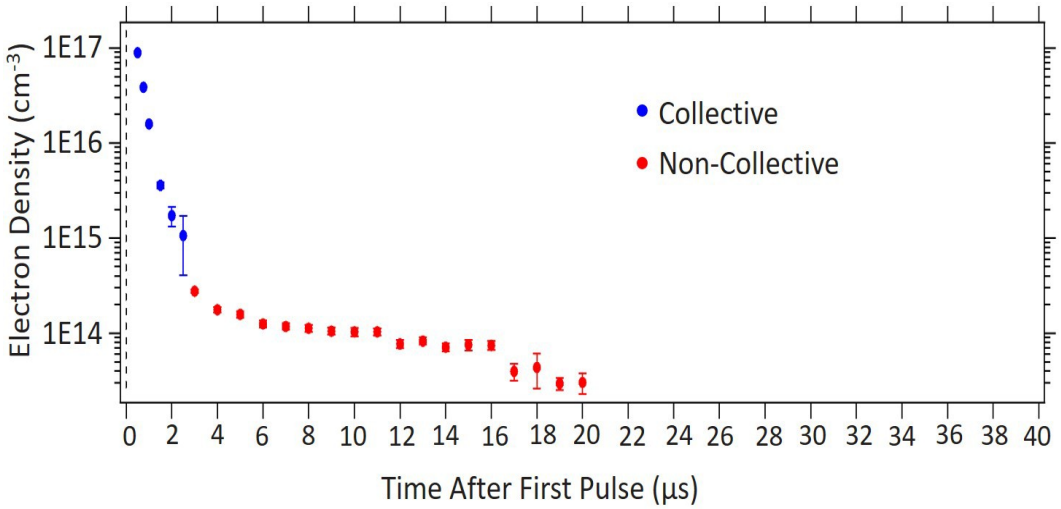

(a)

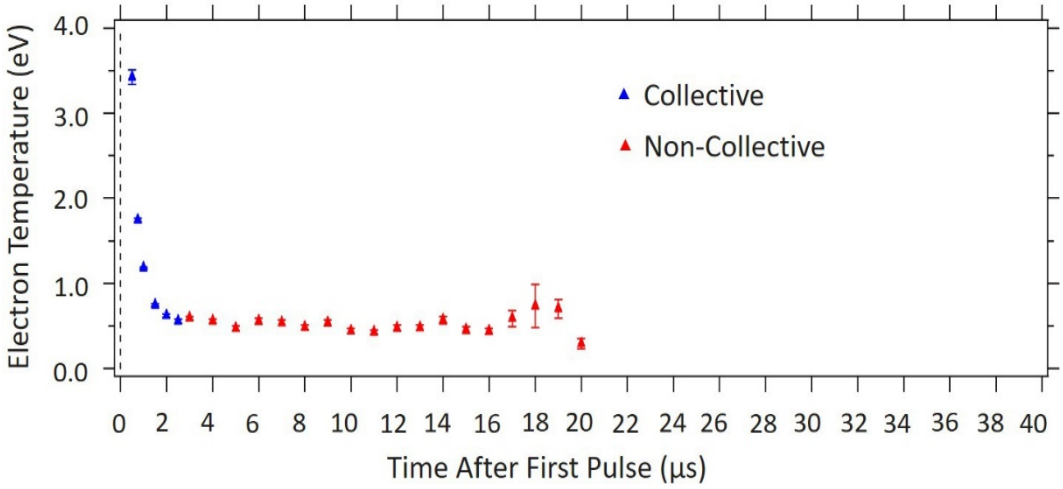

(b)

Figure 22: Electron density (a) and electron temperature (b) measurements of the single nanosecond pulse discharge at various times after the pulse.

Blue markers represent a collective regime, while red markers represent a non-collective regime. Uncertainties differ between collective and non-collective regimes as 10% and 5%, respectively.

In this single pulse burst mode, the collective regime only lasts for roughly 2.5 μs before taking on a more non-collective behavior, as seen by the transition from blue to red data points. During the transition from collective to non-collective, the trend from the output image creates fits with high uncertainty values. As mentioned in Section 5.6, the collective Thomson scattering equations are able to fit to both the collective and non-collective trends, however the fit becomes worse as more of the useful collective scattering spectrum falls under the mask at 532 nm and a transition to non-collective analysis is required. Further in time after the discharge, the rapidly dropping density leads to the signal strength nearing the lower threshold of detection. For the latest data points in both plots, the fits produce measurements with fairly high uncertainties. These plots exhibit rapid changes in both electron density temperature for the first 5 μs, followed by slower cooling and recombination. By 20 μs, the image is interrupted by the rapid refilling of the low density region from nearby air. The density at the earliest measurement point after the

DISTRIBUTION STATEMENT A. Approved for public release. Distribution is unlimited.

discharge is around 10^{17} cm^{-3} and the temperature about 3.5 eV. These earliest measurements were at 500 ns after the pulse and measurements continued up until roughly 20 μs to 25 μs after the final pulse when the uncertainties became large. It is believed that these densities and temperatures would be even higher if measured within the first 500 ns after pulse initiation, but measurements at these early times were not obtainable in this experimental configuration due to the spectral width exceeding that of the detector. Beyond 25 μs, the Thomson scattering signal strength continues to drop and must compete with noise brought in from Raman scattering as N_2 and O_2 refills the low density region.

The two pulse burst mode involves two sequential pulses at 100 kHz with the results of electron density and the electron temperature measurements show in Figures 23a and 23b.

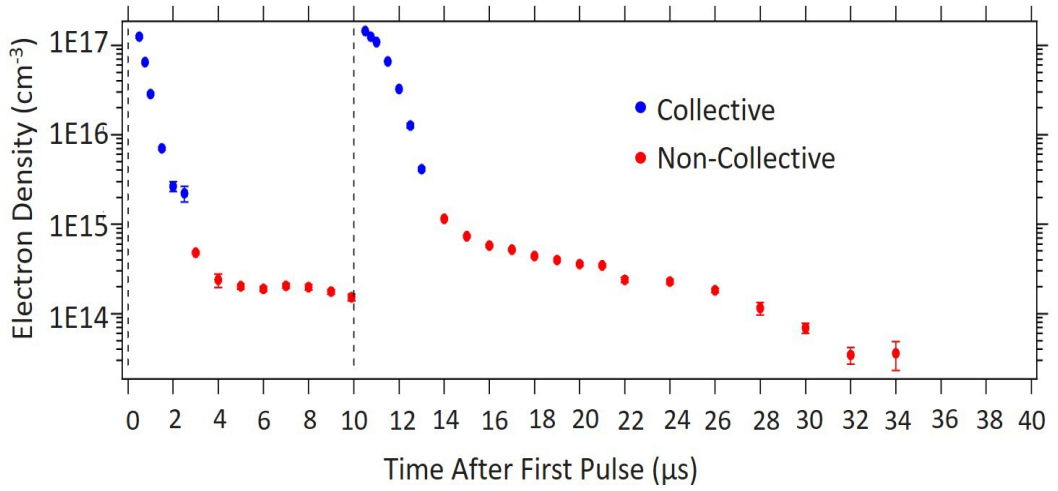

(a)

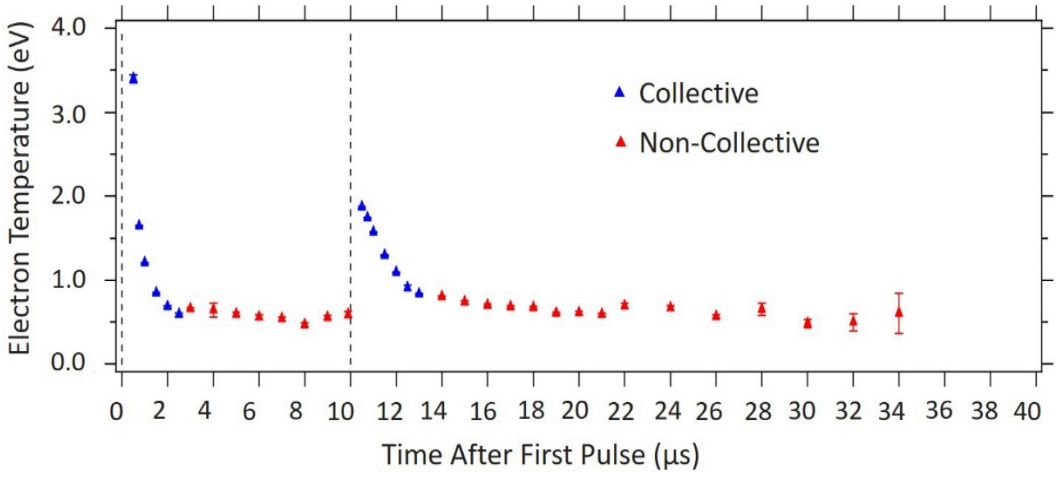

(b)

Figure 23: Electron density (a) and electron temperature (b) measurements with a burst of two pulse discharges at a 100 kHz repetition rate at various times after the initial pulse

Blue markers represent a collective regime, while red markers represent a non-collective regime.

While the behavior after the first of the two pulses is nearly identical to the single pulse burst mode as expected, the second pulse ignites a discharge 10 μs after the initial pulse which

DISTRIBUTION STATEMENT A. Approved for public release. Distribution is unlimited.

interrupts the decaying density and temperature trends. Immediately after the second pulse, the recorded spectra indicate collective behavior once again with even higher densities than after the first pulse. The second pulse appears to be coupled to the first and effectively resets the time before the low density pocket collapses by recirculation. While the subsequent pulse doesn't have as high peak electron temperatures than the initial pulse, these temperatures seem to fall at a much slower rate.

As with the single pulse, higher uncertainties are seen during the transition from collective to non-collective scattering as well as near the end of the data set as signal decreases. Interestingly, the uncertainties found in the second pulse are overall lower than uncertainties from the first pulse. Even for similar alpha values, the trends from the second pulse fit the theoretical trends better.

The four pulse burst mode involved four repetitive pulses at 200 kHz, with the results of electron density and the electron temperature measurements show in Figures 24a and 24b.

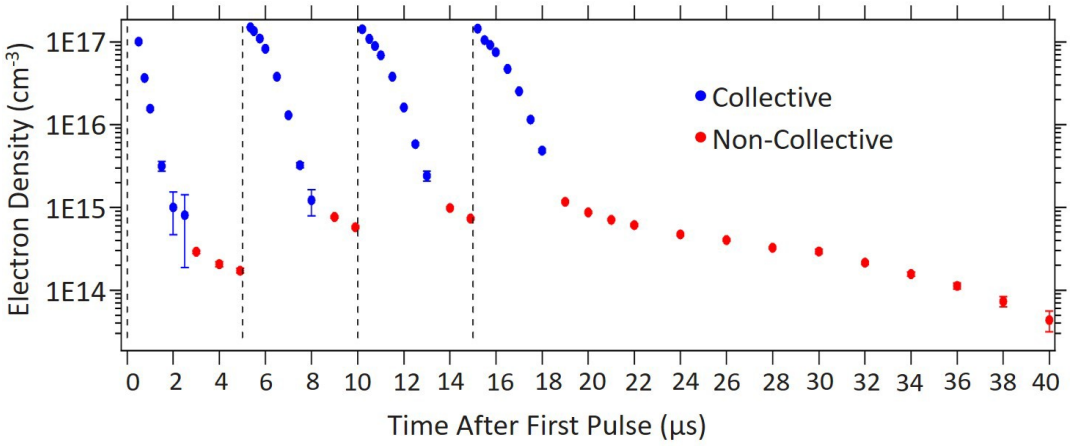

(a)

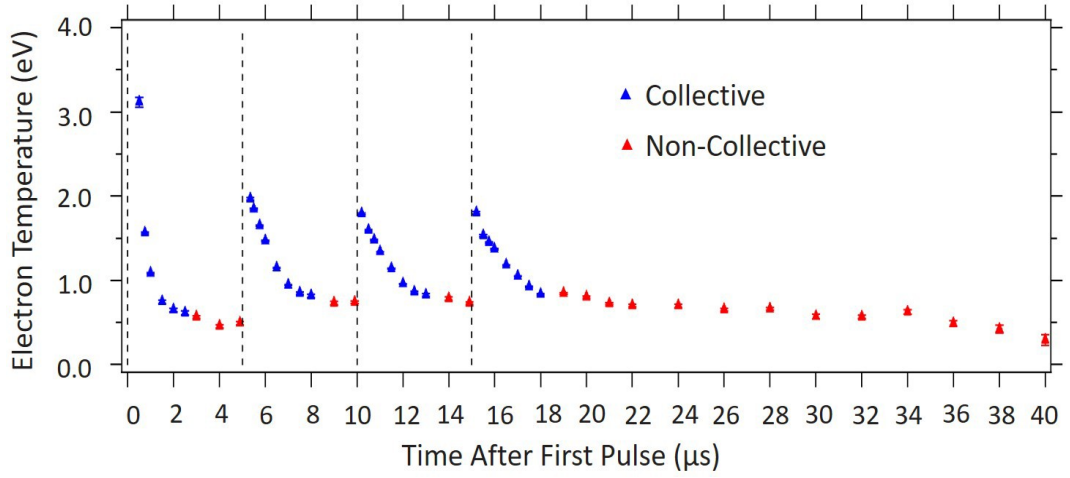

(b)

Figure 24: Electron density (a) and electron temperature (b) measurements for a burst of four pulse discharges at 200 kHz at various times after the initial pulse

Blue markers represent a collective regime, while red markers represent a non-collective regime.

DISTRIBUTION STATEMENT A. Approved for public release. Distribution is unlimited.

As before, the plasma was seen to reignite with each pulse as subsequent pulses were apparently coupled to the previous pulse, each with higher densities than the first pulse and slower electron temperature decays. Again, the additional pulses seem to extend the life of the low density zone by further inhibiting air recirculation.

The data from the three subsequent pulses at first appear very similar to each other, with a similar initial condition being coupled with the previous pulse. However upon closer inspection, it can be determined that each subsequent pulsed discharge resulted in slightly higher densities and temperatures than the previous pulse. The situation seemed to be close to reaching an equilibrium and if many additional pulses would have been added, it is expected that the peak densities and temperatures would not have continued to increase significantly.

Any noticeable differences in measurements between each data sets for the same times after the initial discharge can be possibly attributed to electrode sharpness and alignment to the center of the 2 mm gap. These factors were incorporated into the overall uncertainty analysis. For collective scattering, each data point had an uncertainty of approximately 5% while the non-collective scattering had a larger 10% uncertainty due to a need to fit multiple spectra and a lower overall Thomson scatter intensity. Potential uncertainty contributions from the 7 mJ laser were accounted for with a detailed analysis presented next.

6.2 Effects of Incident Laser Energy on Electron Temperature and Density Measurements

A laser passing through a plasma can potentially cause heating of the plasma as the electrons absorb some of the energy by inverse bremsstrahlung (IB). Sufficiently strong laser intensities and higher frequencies can even ionize atoms, freeing up extra electrons and artificially raising the electron density. To examine the extent by which electrons were being heated or freed due to the laser in this work, electron density and temperature measurement sets were taken with variable incident laser energy per pulse. Separate sets were taken for both the collective, Figure 25, and non-collective, Figure 26, laser scattering regimes.

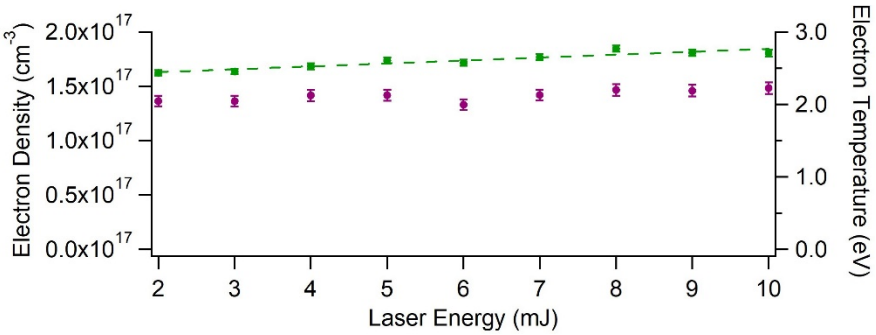

Figure 25: Laser power variation for collective scatter 500 ns after the discharge with electron density (purple) and electron temperature (green) measured

Heating effects on T_e were slight, but significant enough to allow a linear fit trend.

Figure 25 shows no observable change in electron density (purple points) for the laser energy range studied even at the highest densities measured. The electron temperature (green points) shows slight heating with increasing laser energy, but only at the highest densities of the data taken, which correspond to early after the pulse in Figure 24b where $n_e > 10^{17}\text{cm}^{-3}$. This heating

DISTRIBUTION STATEMENT A. Approved for public release. Distribution is unlimited.

trend in Figure 25 represents about a 12% increase in electron temperature for the laser energy used in acquiring the data in this work and then only at the highest n_e conditions. This relatively low degree of heating observed at these plasma densities agrees well with Dzierzega's theoretical work on IB effects, where heating is predicted to be greatly reduced at lower electron densities [22]. An attempt to account for any heating effects in the T_e measurement could have involved backing out T_e at zero energy by extrapolation, but that would have required an additional set of images for each data point found in Figures 22b, 23b, and 24b and even then the rapidly changing portion of the laser power-temperature trend used for corrections would carry with it high uncertainties due to the low signal levels at low laser pulse energies. It also should be noted that an extrapolation from a linear trend in the laser energy range tested could be misleading as the heating trend could actually become non-linear nearer to zero energy [52].

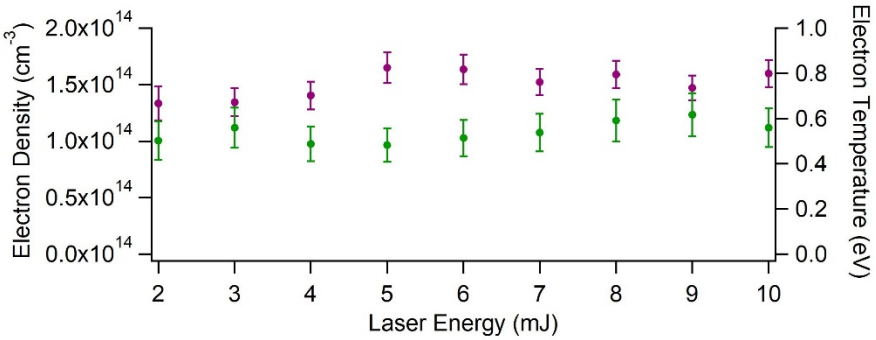

Figure 26: Laser power variation for non-collective scatter 10 μs after the discharge with electron density (purple) and electron temperature (green) measured

No laser effects were observable.

The same process was repeated for sets of electron density and electron temperature measurements with variable laser power shown in Figure 26. Under these non-collective scattering conditions; however, there were no observable changes in electron density or temperature due to laser energy effects.

Due to these considerations, no active corrections were made for laser energy effects on electron density or temperature measurements in this work, except for an acknowledgement that uncertainties in T_e at higher n_e conditions may be a somewhat increased, although still well within a blanket 20% uncertainty across all conditions.

DISTRIBUTION STATEMENT A. Approved for public release. Distribution is unlimited.

7. Conclusion

Time-resolved electron density and temperature measurements were demonstrated in a pin-to-pin nanosecond repetitive pulsed discharge in air at various pulse frequencies using a laser Thomson scattering technique. Electron densities were measured to range from just over 10^{17} cm^{-3} a few hundred nanoseconds after each pulse discharge, decaying toward 10^{14} cm^{-3} after a few microseconds. The n_e decay rate slowed drastically until around 20 μs when air recirculation caused a sudden drop in n_e below detection threshold of about 10^{13} cm^{-3}. Electron temperatures after the initial pulse were found to be elevated at first then decayed rapidly for a few microseconds before stabilizing. Measurements of T_e after subsequent pulse discharges were lower than after the initial pulse but did not decay as rapidly as after the initial pulse, which was an interesting phenomenon that should be investigated in future work. By varying laser pulse energy, it was determined there was little to no effect from laser energy absorption on the measurements of n_e and T_e in this work. These results provide some initial insight on the plasma environment between pulses, which can be difficult to diagnose but very valuable in determining the kinetics during subsequent pulses. Thomson and Raman scattering were shown here to be useful tools in measuring the evolution of plasma parameters between nanosecond repetitive pulsed discharges, albeit a challenging experimental endeavor.

DISTRIBUTION STATEMENT A. Approved for public release. Distribution is unlimited.

8. References

[1] National Research Council. *Plasma Physics of the Local Cosmos*. The National Academies Press, Washington, DC, 2004. ISBN 978-0-309- 09215-9. doi: 10.17226/10993. URL https://www.nap.edu/catalog/10993/ plasma-physics-of-the-local-cosmos.

[2] Yu. R. Alanakyan. Structure of conducting channel of lightning. *Physics of Plas- mas*, 20(8):082106, 2013. doi: 10.1063/1.4817740. URL https://doi.org/10.1063/1. 4817740.

[3] J P Boeuf. Plasma display panels: physics, recent developments and key issues. *Journal of Physics D: Applied Physics*, 36(6):R53–R79, feb 2003. doi: 10.1088/0022-3727/36/6/201. URL https://doi.org/10.1088%2F0022-3727%2F36% 2F6%2F201.

[4] Axel Kramer, Sander Bekeschus, Rutger Matthes, Claudia Bender, Matthias B Stope, Matthias Napp, Olaf Lademann, Jürgen Lademann, Klaus-Dieter Weltmann, and Frieder Schauer. Cold physical plasmas in the field of hygiene relevance, significance, and future applications. *Plasma Processes and Polymers*, 12(12):1410–1422, 2015.

[5] Andrei Vasile Nastuta, Ionut Topala, Constantin Grigoras, Valentin Pohoata, and Gheorghe Popa. Stimulation of wound healing by helium atmospheric pressure plasma treatment. *Journal of Physics D: Applied Physics*, 44(10):105204, 2011.

[6] Francis F Chen. Industrial applications of low-temperature plasma physics. *Physics of Plasmas*, 2(6):2164–2175, 1995.

[7] David B Graves. Plasma processing. *IEEE transactions on Plasma Science*, 22(1): 31–42, 1994.

[8] Steven H. Gold and Gregory S. Nusinovich. Review of high-power microwave source research. *Review of Scientific Instruments*, 68(11):3945–3974, 1997. doi: 10.1063/1.1148382. URL https://doi.org/10.1063/1.1148382.

[9] K Thom, RT Schneider, and FC Schwenk. Physics and potentials of fissioning plasmas for space power and propulsion. *Acta Astronautica*, 3(7-8):505–516, 1976.

[10] N Venkatramani. Industrial plasma torches and applications. *Current Science*, pages 254–262, 2002.

[11] RA Meger, RJ Commisso, G Cooperstein, and Shyke A Goldstein. Vacuum inductive store/pulse compression experiments on a high power accelerator using plasma opening switches. *Applied Physics Letters*, 42(11):943–945, 1983.

[12] Sara Lovascio, Jun Hayashi, Sergey Stepanyan, Gabi D. Stancu, and Christophe O. Laux. Cumulative effect of successive nanosecond repetitively pulsed discharges on the ignition of lean mixtures. *Proceedings of the Combustion Institute*, 37(4):5553 – 5560, 2019. ISSN 1540-7489. doi: https://doi.org/10.1016/j.proci.2018.06.029. URL http://www.sciencedirect.com/science/article/pii/S1540748918302128.

[13] J.J. Thomson. *Conduction of Electricity Through Gases*. Cambridge physical series. University Press, 1903.

[14] A F H van Gessel, E A D Carbone, P J Bruggeman, and J J A M van der Mullen. Laser scattering on an atmospheric pressure plasma jet: disentangling Rayleigh, Raman and Thomson scattering. *Plasma Sources Science and Technology*, 21(1): 015003, February 2012. ISSN 0963-0252, 1361-6595. doi: 10.1088/0963-0252/21/ 1/015003. URL http://stacks.iop.org/0963-0252/21/i=1/a=015003?key=crossref. e16a00ad074075da0945bb1f1b69bff7.

[15] C. M. Penney, R. L. St. Peters, and M. Lapp. Absolute rotational raman cross sections for n2, o2, and co2. *J. Opt. Soc. Am.*, 64(5):712–716, May 1974. doi:

DISTRIBUTION STATEMENT A. Approved for public release. Distribution is unlimited.

10.1364/JOSA.64.000712. URL http://www.osapublishing.org/abstract.cfm?URI= josa-64-5-712.
[16] John David Jackson. *Classical electrodynamics*. Wiley, New York, NY, 3rd ed. edition, 1999. ISBN 9780471309321. URL http://cdsweb.cern.ch/record/490457.
[17] S L Prunty. A primer on the theory of thomson scattering for high-temperature fusion plasmas. *Physica Scripta*, 89(12):128001, nov 2014. doi: 10.1088/0031-8949/89/12/128001. URL https://doi.org/10.1088%2F0031-8949%2F89%2F12%2F128001.
[18] J. Sheffield, D. Froula, S.H. Glenzer, and N.C. Luhmann. *Plasma Scattering of Electromagnetic Radiation: Theory and Measurement Techniques*. Elsevier Science, 2010. ISBN 9780080952031.
[19] M.J. Sande, van de. *Laser scattering on low temperature plasmas : high resolu- tion and stray light rejection*. PhD thesis, Department of Applied Physics, 2002. Proefschrift.
[20] E. E. Salpeter. Electron Density Fluctuations in a Plasma. *Physical Review*, 120 (5):1528–1535, December 1960. ISSN 0031-899X. doi: 10.1103/PhysRev.120.1528. URL https://link.aps.org/doi/10.1103/PhysRev.120.1528.
[21] A. Bogaerts, E. Neyts, R. Gijbels, and J.J.A.M. Mullen, van der. Gas discharge plasmas and their applications. *Spectrochimica Acta. Part B : Atomic Spectroscopy*, 57(4):609–658, 2002. ISSN 0584-8547. doi: 10.1016/S0584-8547(01)00406-2.
[22] Krzysztof Dzierga, Witold Zawadzki, Bartomiej Pokrzywka, and Stephane Pellerin. Experimental investigations of plasma perturbation in Thomson scattering applied to thermal plasma diagnostics. *Physical Review E*, 74(2):026404, August 2006. ISSN 1539-3755, 1550-2376. doi: 10.1103/PhysRevE.74.026404. URL https://link.aps.org/doi/10.1103/PhysRevE.74.026404.
[23] A. V. Phelps and Z. Lj Petrovic. REVIEW ARTICLE: Cold-cathode discharges and breakdown in argon: surface and gas phase production of secondary electrons. *Plasma Sources Science Technology*, 8(3):R21–R44, August 1999. doi: 10.1088/ 0963-0252/8/3/201.
[24] A Roettgen, I Shkurenkov, M Simeni Simeni, I V Adamovich, and W R Lem- pert. Time-resolved electron temperature and electron density measurements in a nanosecond pulse filament discharge in H_2 He and O_2 He mixtures. *Plasma Sources Science and Technology*, 25(5):055008, August 2016. ISSN 1361-6595. doi: 10.1088/0963-0252/25/5/055008. URL http://stacks.iop.org/0963-0252/25/i=5/a=055008?key=crossref.3c2e3ef4bfe4ce5b421ba91fd211555f.
[25] D. J. Emmons and D. E. Weeks. Kinetics of high pressure argon-helium pulsed gas discharge. *Journal of Applied Physics*, 121(20):203301, 2017. doi: 10.1063/1. 4983678. URL https://doi.org/10.1063/1.4983678.
[26] A Fridman, A Chirokov, and A Gutsol. Non-thermal atmospheric pressure discharges. *Journal of Physics D: Applied Physics*, 38(2):R1–R24, jan 2005. doi: 10.1088/0022-3727/38/2/r01. URL https://doi.org/10.1088%2F0022-3727%2F38% 2F2%2Fr01.
[27] A. Schutze, J. Y. Jeong, S. E. Babayan, Jaeyoung Park, G. S. Selwyn, and R. F. Hicks. The atmospheric-pressure plasma jet: a review and comparison to other plasma sources. *IEEE Transactions on Plasma Science*, 26(6):1685–1694, 1998.
[28] Y.P. Raizer, V.I. Kisin, and J.E. Allen. *Gas Discharge Physics*. Springer Berlin Heidelberg, 2011. ISBN 9783642647604. URL https://books.google.com/books?id= zd-KMAEACAAJ.
[29] David Z. Pai, Deanna A. Lacoste, and Christophe O. Laux. Transitions between corona,

DISTRIBUTION STATEMENT A. Approved for public release. Distribution is unlimited.

glow, and spark regimes of nanosecond repetitively pulsed discharges in air at atmospheric pressure. *Journal of Applied Physics*, 107(9):093303, 2010. doi: 10.1063/1.3309758. URL https://doi.org/10.1063/1.3309758.

[30] Ronny Brandenburg, Peter J Bruggeman, and Svetlana M Starikovskaia. Fast pulsed discharges. *Plasma Sources Science and Technology*, 26(2):020201, jan 2017. doi: 10.1088/1361-6595/aa5205. URL https://doi.org/10.1088%2F1361-6595%2Faa5205.

[31] Charles H. Kruger, Christophe O. Laux, Lan Yu, Denis M. Packan, and Laurent Pierrot. Nonequilibrium discharges in air and nitrogen plasmas at atmospheric pressure. *Pure and Applied Chemistry*, 74(3):337–347, January 2002. ISSN 1365-3075, 0033-4545. doi: 10.1351/pac200274030337. URL http://www.degruyter.com/view/ j/pac.2002.74.issue-3/pac200274030337/pac200274030337.xml.

[32] Jonathan M. Bonebrake, David L. Blunck, Joseph K. Lefkowitz, and Timothy M. Ombrello. The effect of nanosecond pulsed high frequency discharges on the temperature evolution of ignition kernels. *Proceedings of the Combustion Institute*, 37(4):5561– 5568, 2019. ISSN 1540-7489. doi: https://doi.org/10.1016/j.proci.2018.06.027. URL http://www.sciencedirect.com/science/article/pii/S1540748918302104.

[33] Maria Castela, Sergey Stepanyan, Benoit Fiorina, Axel Coussement, Olivier Gicquel, Nasser Darabiha, and Christophe O. Laux. A 3-d dns and experimental study of the effect of the recirculating flow pattern inside a reactive kernel produced by nanosecond plasma discharges in a methane-air mixture. *Proceedings of the Combustion Institute*, 36(3):4095 – 4103, 2017. ISSN 1540-7489. doi: https://doi.org/10.1016/j.proci.2016.06.174. URL http://www.sciencedirect.com/ science/article/pii/S154074891630236X.

[34] Joseph K. Lefkowitz, Peng Guo, Timothy Ombrello, Sang Hee Won, Christopher A. Stevens, John L. Hoke, Frederick Schauer, and Yiguang Ju. Schlieren imaging and pulsed detonation engine testing of ignition by a nanosecond repetitively pulsed discharge. *Combustion and Flame*, 162(6):2496 – 2507, 2015. ISSN 0010-2180. doi: https://doi.org/10.1016/j.combustflame.2015.02.019. URL http://www.sciencedirect.com/science/article/pii/S001021801500070X.

[35] David Alderman, Christopher Tremble, Dan Singleton, Jason Sanders, and Chunqi Jiang. Effects of pulse rise time and repetition frequency on nanosecond pulsed plasma ignition for combustion. *Plasma Research Express*, 2020. URL http://iopscience.iop.org/10.1088/2516-1067/ab880a.

[36] G. Hebner, P. Miller, and J. Woodworth. *Overview of Plasma Diagnostic Techniques*, pages 145–204. 01 2000. ISBN 978-3-642-63096-5. doi: 10.1007/978-3-642-56989-0 5.

[37] V A Godyak and V I Demidov. Probe measurements of electron-energy distributions in plasmas: what can we measure and how can we achieve reliable results? *Journal of Physics D: Applied Physics*, 44(23):233001, may 2011. doi: 10.1088/0022-3727/44/ 23/233001. URL https://doi.org/10.1088%2F0022-3727%2F44%2F23%2F233001.

[38] D L Crintea, U Czarnetzki, S Iordanova, I Koleva, and D Luggenhlscher. Plasma diagnostics by optical emission spectroscopy on argon and comparison with thomson scattering. *Journal of Physics D: Applied Physics*, 42(4):045208, jan 2009. doi: 10. 1088/0022-3727/42/4/045208. URL https://doi.org/10.1088%2F0022-3727%2F42% 2F4%2F045208.

[39] Andrew T. Young. Rayleigh scattering. *Physics Today*, 35(1):42–48, 1982. doi: 10.1063/1.2890003. URL https://doi.org/10.1063/1.2890003.

[40] A B Murphy and A J D Farmer. Temperature measurement in thermal plasmas by rayleigh scattering. *Journal of Physics D: Applied Physics*, 25(4):634–643, apr 1992. doi:

DISTRIBUTION STATEMENT A. Approved for public release. Distribution is unlimited.

10.1088/0022-3727/25/4/009. URL https://doi.org/10.1088%2F0022-3727%2F25%2F4%2F009.

[41] S F Adams, J E Caplinger, and B S Sommers. Spatial temperature mapping of an atmospheric microdischarge using ultraviolet rayleigh scatter imaging. *Plasma Sources Science and Technology*, 24(2):025031, apr 2015. doi: 10.1088/0963-0252/ 24/2/025031. URL https://doi.org/10.1088%2F0963-0252%2F24%2F2%2F025031.

[42] Xingxing Wang, Paul Stockett, Ravichandra Jagannath, Sally Bane, and Alexey Shashurin. Time-resolved measurements of electron density in nanosecond pulsed plasmas using microwave scattering. *Plasma Sources Sci. Technol.*, 27(7):07LT02, July 2018. ISSN 1361-6595. doi: 10.1088/1361-6595/aacc06. URL http://stacks.iop.org/0963-0252/27/i=7/a=07LT02?key=crossref. b52c7027ae80ec0e056803f14b5e91db.

[43] Vladlen Podolsky, Andrei Khomenko, and Sergey Macheret. Time-resolved measurements of electron number density in argon and nitrogen plasmas sustained by high-voltage, high repetition rate, nanosecond pulses. *Plasma Sources Science and Technology*, 27(10):10LT02, October 2018. ISSN 1361-6595. doi: 10.1088/ 1361-6595/aae35e. URL http://stacks.iop.org/0963-0252/27/i=10/a=10LT02?key=crossref.b10abe5fcd226fbab7524137a14ca27d.

[44] D. W. Phillion, D. L. Banner, E. M. Campbell, R. E. Turner, and K. G. Estabrook. Stimulated raman scattering in large plasmas. *The Physics of Fluids*, 25(8):1434–1443, 1982. doi: 10.1063/1.863920. URL https://aip.scitation.org/doi/abs/10.1063/ 1.863920.

[45] M. Minnaert. On the continuous spectrum of the corona and its polarisation. With 3 figures. (Received July 30, 1930). *Zeitschrift fuer Astrophysik*, 1:209, January 1930.

[46] H. C. van de Hulst. The electron density of the solar corona. *Bulletin Astronomical Institute of the Netherlands*, 11:135, February 1950.

[47] D E Evans and J Katzenstein. Laser light scattering in laboratory plasmas. *Reports on Progress in Physics*, 32(1):207–271, jan 1969. doi: 10.1088/0034-4885/32/1/305. URL https://doi.org/10.1088%2F0034-4885%2F32%2F1%2F305.

[48] N. J. Peacock, D. C. Robinson, M. J. Forrest, P. D. Wilcock, and V. V. Sannikov. Measurement of the Electron Temperature by Thomson Scattering in Tokamak T3. *Nature*, 224(5218):488–490, November 1969. ISSN 0028-0836, 1476-4687. doi: 10.1038/224488a0. URL http://www.nature.com/articles/224488a0.

[49] S Hbner, J Santos Sousa, V Puech, G M W Kroesen, and N Sadeghi. Electron properties in an atmospheric helium plasma jet determined by Thomson scattering. *Journal of Physics D: Applied Physics*, 47(43):432001, October 2014. ISSN 0022-3727, 1361-6463. doi: 10.1088/0022-3727/47/43/432001. URL http://stacks.iop.org/ 0022-3727/47/i=43/a=432001?key=crossref.49d5428c73d305e0e576caac7bad4ef8.

[50] C Jiang, J Miles, J Hornef, C Carter, and S Adams. Electron densities and temperatures of an atmospheric-pressure nanosecond pulsed helium plasma jet in air. *Plasma Sources Science and Technology*, 28(8):085009, August 2019. ISSN 1361- 6595. doi: 10.1088/1361-6595/ab2182. URL https://iopscience.iop.org/article/10. 1088/1361-6595/ab2182.

[51] E A D Carbone, J M Palomares, S Hbner, E Iordanova, and J J A M van der Mullen. Revision of the criterion to avoid electron heating during laser aided plasma diagnostics (LAPD). *Journal of Instrumentation*, 7(01):C01016–C01016, jan 2012. doi: 10.1088/1748-0221/7/01/c01016. URL https://doi.org/10.1088% 2F1748-0221%2F7%2F01%2Fc01016.

DISTRIBUTION STATEMENT A. Approved for public release. Distribution is unlimited.

[52] A. B. Murphy. Thomson scattering diagnostics of thermal plasmas: Laser heating of electrons and the existence of local thermodynamic equilibrium. *Phys. Rev. E*, 69:016408, Jan 2004. doi: 10.1103/PhysRevE.69.016408. URL https://link.aps.org/doi/10.1103/PhysRevE.69.016408.

[53] Steven Adams, Jared Miles, Timothy Ombrello, Russell Brayfield, and Joseph Lefkowitz. The effect of inter-pulse coupling on gas temperature in nanosecond-pulsed high-frequency discharges. *J. Phys. D: Appl. Phys.*, 52(35):355203, Au- gust 2019. ISSN 0022-3727, 1361-6463. doi: 10.1088/1361-6463/ab27ef. URL https://iopscience.iop.org/article/10.1088/1361-6463/ab27ef.

DISTRIBUTION STATEMENT A. Approved for public release. Distribution is unlimited.